

Research Paper

A new lift model for Euler–Lagrange large eddy simulation of turbulent bubble plumes

Mohammad Karimi Zand ^{a,b}, Simon Innerbichler ^b, Stefan Puttinger ^b, Mahdi Saeedipour ^b,* 

^a K1-MET Metallurgical Competence Center, Stahlstraße 14, 4020 Linz, Austria

^b Department of Particulate Flow Modelling, Johannes Kepler University, A-4040 Linz, Austria

ARTICLE INFO

Keywords:

Bubble dynamics
Bubble lift
Vorticity
Plume hydrodynamics
Bubble column
Large eddy simulation
Turbulence

ABSTRACT

Most Euler–Lagrange simulations of bubbly flows employ lift force models derived from single-bubble hydrodynamics, which are insufficient for predicting macroscopic quantities of such complex systems. In this study, we propose a novel physics-based lift model for turbulent bubble plumes, which is applicable for the Euler–Lagrange large eddy simulation (LES). Based on physical observations from single-phase free jets, it is hypothesized that the bubble plume lateral spreading can be characterized by global and local turbulent properties resolved in LES. Accordingly, a dimensionless parameter β_L is defined based on turbulence decay time, vorticity time scale, gas volume fraction, and bubble Eotvos number, which are incorporated in the formulation of a new lift force model. The performance of the proposed model was evaluated against different conventional lift models derived from single-bubble hydrodynamics using various experimental benchmarks from the literature as well as an in-house experiment. These benchmarks cover bubble plumes with mono- and poly-disperse bubbles in the size range of 0.5–11 mm. The results clearly show that the proposed model outperforms the conventional models in predicting macroscopic characteristics of bubble plume, such as time-averaged velocity profiles and gas holdup. Further statistical analysis based on the PDF of bubble velocities demonstrates that the proposed model more accurately predicts the lateral dispersion of the plume. These results highlight the potential of the new model for more accurate simulation of bubble plume dynamics in large-scale industrial applications.

1. Introduction

Whether it is waste water treatment, pool scrubbing in nuclear powerplants, manufacturing of pharmaceutical products, mineral flotation or non-metallic inclusion removal in steel, bubbly flows are used in a variety of industrial processes. The use of multiphase bubbly flows in the process oriented systems such as bubble columns, bubble curtains, or bubble plumes offers several advantages over other mechanical methods due to their unique features such as low maintenance costs and ease of use. Evidently, thorough understanding of their complicated nature is not only beneficial, but also essential for optimizing their application in these processes. Hence, researchers have been investigating bubbly flows inherent parameters which are influential in the flow regime, operational efficiency, and robustness. Some of these important parameters are gas and liquid flux, bubble dispersion rate, and gas hold-up (Zakari et al., 2025; Besagni and Inzoli, 2016; Hessenkemper et al., 2021). For several decades, researchers had been using experiments to study the bulk flow behavior of these multiphase flows to analyze the hydrodynamic behavior of bubble columns and

bubble plumes (Laupsien et al., 2022; Simonnet et al., 2007; Lucas et al., 2006), and during the past few decades, Computational Fluid Dynamics (CFD) has become a valuable tool for researchers to study the integral and local flow properties of bubble plumes and bubble columns and high-fidelity simulation techniques like Direct Numerical Simulation (DNS) have proven most helpful with small scale highly detailed investigations (Zhang et al., 2006; Fraga et al., 2016; Buwa et al., 2006; Zhang et al., 2020; Tryggvason and Lu, 2015). While experimental investigations are also extensively used for detailed local flow behavior analyses, they usually need expensive equipment and considerable care in measurements in order to achieve accurate results (Martínez Mercado et al., 2010; Wu et al., 2021; Seol et al., 2007). CFD simulations, on the other hand, provide the convenience of use with the advent of computationally more capable CPUs and faster simulation models like Euler–Euler and Euler–Lagrange models, which are mainly used for large-scale industrial applications. Nevertheless, these simulations require correct interface force modeling and incisive closure of the momentum equations to deliver accurate results, and

* Corresponding author.

E-mail address: mahdi.saeedipour@jku.at (M. Saeedipour).

<https://doi.org/10.1016/j.ijmultiphaseflow.2026.105722>

Received 2 February 2026; Received in revised form 24 March 2026; Accepted 2 April 2026

Available online 5 April 2026

0301-9322/© 2026 The Authors. Published by Elsevier Ltd. This is an open access article under the CC BY license (<http://creativecommons.org/licenses/by/4.0/>).

these models require validation from the experimental results (Lucas et al., 2007; Buwa and Ranade, 2002; Zhang and Zhang, 2022). Therefore, in many studies, investigations conducted around bubbly flows are combined experimental and numerical investigations.

When using numerical simulation methods like Euler–Euler and Euler–Lagrange, there are multiple closure models that should be used for resolving the flow correctly. In the context of bubbly flow simulations, these models include, but are not limited to, the drag force, the virtual mass force, the lateral lift force, and the gravity force, which is the main drive for bubble buoyancy. Some of the other closures, like bubble coalescence and breakup models, are also used recurrently when a more sophisticated depiction of the process is required. The lateral lift force, which is imposed on the bubble perpendicular to its rise path, is the predominant influencing factor on the lateral distribution of the bubbles in a plume or column setting (Legendre and Magnaudet, 1998). The bubble lateral distribution is a major influencing factor in many industrial processes, as it promotes mixing and bubble-particle interaction, which are required for an effective and optimal performance (Shu et al., 2019). Clearly, a comprehensive understanding of the lift force phenomenon brings a correct definition of the force modeling, which will subsequently result in an accurate depiction of the flow hydrodynamics in bubbly flow simulations.

Many studies have conducted valuable investigations of the bubble lateral lift force and shed light on the complex nature of this force. According to these studies, the emergence of the lift force is caused by the vorticity of the flow, which is also evident in its formulation (Auton, 1987). In the case of bubble plumes, this rotational disturbance of the flow, namely the vorticity, is caused by the bubble plume itself (Lucas et al., 2006). Depending on the voidage profile of the plume, the liquid flow can have a range of velocity profiles. Non-uniform distribution of the gas phase, usually having peak values at the center of the plume, results in more liquid entrainment at the center that can closely represent a Poiseuille flow profile. According to the results of Tomiyama et al. (2002), the direction of lift force is determined by the lift coefficient, C_L . Negative values of C_L mean that the bubbles are moving towards the regions of the flow with higher velocity, and positive values mean that the bubbles are moving towards the regions with lower background velocity, i.e., in a plume setting, the center of the plume and the walls, respectively. Although the sign change of the lift force is a highly debated topic in the literature, and different studies have explained this lift reversal phenomenon through different perspectives, most of the available results have observed that the direction change of the bubble happens when the bubble shape starts to deform (Tomiyama et al., 2002; Adoua et al., 2009; Zand et al., 2025). Generalized depiction of the lift coefficient has proven difficult to attain, and numerous lift coefficient models have been developed in the past decades. Auton (1987) reported a constant value of 0.5 for C_L in their article using analytical derivation. This study was carried out for spherical single bubbles rising in non-viscous linear shear flows. Legendre and Magnaudet (1998) did a comprehensive direct numerical simulation by fully resolving the Navier–Stokes equation around a spherical bubble moving in a viscous linear shear flow, and calculated the lift coefficient in different conditions. They provided a model that no longer had a constant value for C_L , and was a function of the dimensionless shear rate and bubble Reynolds number. Their formulation only showed positive values for C_L ; nonetheless, they only focused on spherical bubbles. Tomiyama et al. (2002) introduced the first lift coefficient model that considered bubble deformation in the formulation. They used a rotating shear belt experimental setup to trace the path of bubbles having different sizes and calculated the lift force using the bubble trajectories, which later became one of the most used lift models to this day. In the work of Adoua et al. (2009), it was proven that the lift model proposed by Legendre and Magnaudet (1998) gives accurate results for spherical single bubbles, but it lacks the explanation for deformed bubbles. It was also explained that the reversal of the lift force is due to vorticity generation at the immediate

vicinity of deformed bubbles. Hassenkemper et al. (2021) conducted a large number of experiments on single bubbles having different sizes rising in water. They used an auxiliary bubble column, which imposed a rotational flow field in the liquid, to study the effect of different shear rates on the bubble. The proposed model was a combination of the lift model of Legendre and Magnaudet (1998) with an added bubble deformation effect. More recently, Hayashi et al. (2021) used the same experimental dataset to add the effect of vorticity generation at the bubble surface to the (Legendre and Magnaudet, 1998) model.

Among all of the lift coefficient models available in the literature, very few of them have studied C_L in either an experimental set or a numerical simulation of bubble column/plume, and all of the studies mentioned previously have investigated bubble C_L in a single bubble setup, where weak shear assumptions are valid and the dimensionless shear rate value is less than 1 (Auton, 1987; Legendre and Magnaudet, 1998). In the case of bubble drag force, many researchers have studied the drag closure models for single bubbles and particles. More recent studies have argued that the drag force in a bubble swarm is different from the drag imposed on a single bubble, and derived drag models by actuating a multi-bubble set of experiments or simulations (Simonnet et al., 2007). Regarding lateral distribution of bubbles, which in turn influences the radial liquid velocity profile, some researchers have reported discrepancies compared to experimental results when employing available lift models in simulations (Zhang et al., 2006; Subburaj et al., 2023). Although researchers have related this deviation of bubble radial distribution to the selection of a physically sound collision model for gas bubbles (Xue et al., 2017), the recent work of Subburaj et al. (2023) demonstrates that a correct collision force combined with conventional single bubble-based lift force model still fails to simulate the correct liquid velocity profile for different plumes and different heights of the plume. Sokolichin et al. (2004) has indicated that a lift coefficient model for bubbles rising in a swarm is lacking in the literature. They have also highlighted that C_L values, which are to be used in numerical simulations of bubble swarm flows, e.g. bubble plumes, should have been derived from buoyancy-driven flow studies in which multiple bubbles are present. Hibiki and Ishii (2007) have also pointed out that, in the same manner as drag force, bubble lift force is also dependent on whether the flow consists of a single or multiple bubbles, as the presence of other bubbles not only influences the movement of the bubble, but also drastically changes the properties of the liquid flow. Determination of the drag coefficient is more straightforward since the drag force mostly depends on the bubble Reynolds number, but the lift force seems to be influenced by many other factors, such as Reynolds number, liquid viscosity, and shear rate. Bubbles rising in turbulent swarms are often exposed to more complex interaction mechanisms with the turbulence and the other bubbles. These interactions are caused either by the turbulent flow or by the bubbles themselves, such as the wake-induced oscillations in the domain as well as anisotropy in turbulence that eventually enhance both horizontal or vertical bubble dispersion and drastically change the radial distribution of bubbles rising in a swarm (Huang et al., 2025; Mathai et al., 2018; Maeda et al., 2021). It is worth mentioning that in the case of a two-phase bubbly flow, the upwards-directed anisotropic turbulence is caused by the bubble-induced turbulence, and can draft the trailing bubbles upwards in a ballistic regime as shown in the work of Huang et al. (2025), which increases the vertical dispersion of the bubbles drastically, and even dampens the horizontal dispersion of the bubble. This effect is even more pronounced when bubble-induced turbulence is higher in the system with larger bubble sizes in the swarm. On the other hand, leading bubble wake can cause horizontal ejection of the trailing bubble which leads to lateral dispersion, as shown in Maeda et al. (2021). These complexities bring out more ambiguity in the assignment of the lift coefficient for a bubbly flow system (Hibiki and Ishii, 2007; Sokolichin et al., 2004). Some researchers have even tried to derive stochastic models for bubble dispersion in turbulence (Lain et al., 2002) which remain beyond the scope of the current study. In an extensive

experimental study, Kulkarni (2008) calculated the lift coefficient of different bubble sizes rising in a bubble column using instantaneous velocities of the bubbles. The results showed variations in C_L with the single bubble model of Tomiyama et al. (2002) not only in the values, but also in the onset of lift reversal. They also proposed a C_L model based on local turbulent kinetic energy and void fraction of the bubble column. Their C_L values changes not only along the column axis, but also along the radius of the bubble column. Sugrue (2017) also proposed a lift coefficient for bubbly systems by correlating the C_L to gas voidage and turbulence intensity. Salibindla et al. (2020) studied the drag and lift coefficients of deformable single bubbles in turbulence experimentally. Interestingly, they found out that the direction change of bubble lateral migration in intense turbulence happens at a much smaller diameter compared to what is believed based on studies of single bubbles rising in a laminar flow. In a more recent work, Subburaj et al. (2023) used Computational Fluid Dynamics coupled with Discrete Element Method (Euler–Lagrange) to study the effect of lift model on gas dispersion in a bubble plume. They compared the results with experiments of Deen (2001), and found that the use of a constant lift coefficient, which is derived using single bubble analyses, does not replicate the whole dynamic range of the plume, and the lift coefficient should change based on flow properties. They defined a C_L based on gas volume fraction and dimensionless shear rate, which is responsive to the local flow properties of the bubbly flow.

The present literature review confirms that several aspects of lift force modeling in bubbly flows still remain unresolved, and single-bubble-derived correlations are not sufficient for the prediction of such complex systems. In particular, the dynamics of the plume and the presence of the other bubbles should be included in the lift force. Therefore, the present study investigates the dependence of the bubble C_L on the dynamics of turbulent flow, and proposes a physical model that explicitly relies on local turbulence characteristics. In reference to our previous work (Zand et al., 2025), in which we have comprehensively explained that vorticity is the key mechanism behind the emergence of the single bubble lift force, this work will delve further into the role of turbulence and local vorticity on bubble lateral migration in bubbly plumes. We employ these concepts to propose an explicit lift model applicable to Euler–Lagrange LES, which is further validated with various experiments. This article is structured as follows: in Section 2, the Euler–Lagrange framework is introduced for modeling bubbly flows. Section 3 explains the importance of lift force modeling in bubbly flow simulations and elucidates the motivation for defining a new lift model. In this section, the theoretical basis of the newly proposed model, and the cases studied in this work are explained in detail. Section 4 evaluates the model performance by comparing to other lift models and experimental results. The article ends with conclusions and suggestions for future work in Section 5.

2. Euler–Lagrange framework for bubbly flows

To study the flow dynamics and bubble behavior in the present work, unresolved Euler–Lagrange simulations were conducted in a four-way coupled Euler–Lagrange approach. This method, combines Computational Fluid Dynamics to treat the liquid phase as the continuum, and the Discrete Element Method to treat the gas bubbles as the discrete phase. The four-way coupling between the two phases is achieved via incorporating the dispersed phase fraction in the CFD equations, the momentum transfer between the phases, and the collision forces between the parcels. This coupled framework enables a consistent treatment of interphase momentum transfer and accurately represents both large-scale liquid motion and small-scale bubble dynamics. The open source solver OpenFOAM was selected for these numerical simulations. It should be noted that the solver used for the CFD is based on the Volume of Fluid method (VOF) which can have two continuous phases at the same time (water and air in our case). This can add a gas–liquid free surface at the top of the plume. The equations solved for the simulations carried out in this work are presented in the following sections.

2.1. Computational fluid dynamics

As mentioned before, the liquid phase is treated as a continuous medium, and its governing equations are derived from the volume-averaged Navier–Stokes equations. The governing equations, which consist of continuity and momentum equations, are as follows:

$$\frac{\partial}{\partial t} (\phi_c \rho_c) + \nabla \cdot (\phi_c \rho_c \mathbf{u}) = 0 \quad (1)$$

$$\frac{\partial}{\partial t} (\phi_c \rho_c \mathbf{u}) + \nabla \cdot (\phi_c \rho_c \mathbf{u} \mathbf{u}) = -\phi_c \nabla p + \phi_c \rho_c \mathbf{g} + \nabla \cdot (\phi_c \boldsymbol{\tau}) - \sum_{i=1}^n \frac{\mathbf{F}_i^d}{V_{\text{cell}}} \quad (2)$$

In these equations, ϕ_c is the volume fraction of the continuous phase, ρ_c is the density, \mathbf{u} is the velocity vector, p is the pressure term, \mathbf{g} is the gravitational acceleration, and $\boldsymbol{\tau}$ is the stress tensor for the continuous phase. This term can be written as:

$$\boldsymbol{\tau} = \mu_{\text{eff}} \left(\nabla \mathbf{u} + (\nabla \mathbf{u})^T - \frac{2}{3} \mathbf{I} (\nabla \cdot \mathbf{u}) \right) \quad (3)$$

where μ_{eff} is the effective viscosity. In the context of turbulence modeling techniques, including LES, the viscosity term consists of the molecular viscosity of the continuous phase and the subgrid scale (SGS) eddy viscosity i.e. $\mu_{\text{eff}} = \mu_c + \mu_{\text{sgs}}$. The latter is the main step in modeling SGS stresses and proposing closures for the spatially-filtered equations. In this study, we only focus on modeling the convective SGS term in the filtered Navier–Stokes equations, and employ a functional one-equation subgrid model based on the subgrid turbulent kinetic energy (Yoshizawa, 1986), which reads

$$\mu_{\text{sgs}} = \rho_c C_k \Delta k_{\text{sgs}}^{1/2}. \quad (4)$$

This model depends on the density of the continuous phase ρ_c , the LES filter size Δ , that is approximated with the grid resolution, a model constant C_k , and the turbulent kinetic energy of the subgrid k_{sgs} , for which an additional transport equation is solved.

It has to be noted that the choice of LES for treating turbulence allows us to define local turbulent quantities that are instantly accessible in each finite volume cell. This would be beneficial for developing physical models for the Euler–Lagrange simulation that are based on *scale-resolved* picture of the turbulence, rather than its time-averaged characteristics. Accordingly, resolved turbulent kinetic energy and resolved dissipation rate can be computed from the LES-resolved velocity field in an *a-posteriori* manner. Therefore, a Laplacian-based spatial filter was applied to the instantaneous velocity field to separate the resolved fluctuations from the large-scale motion, such that $\mathbf{u}' = \mathbf{u} - \bar{\mathbf{u}}$, where \mathbf{u} is the instantaneous velocity field, $\bar{\mathbf{u}}$ denotes the filtered velocity obtained using a Laplace filter, and \mathbf{u}' represents the resolved velocity fluctuations. This definition allows us to calculate a resolved turbulent kinetic energy as

$$k_{\text{res}} = \frac{1}{2} |\mathbf{u}'|^2, \quad (5)$$

and a resolved turbulent dissipation rate is evaluated as

$$\epsilon_{\text{res}} = 2\nu |\mathbf{S}_{\text{res}}|^2, \quad (6)$$

where ν is the kinematic viscosity of the continuous phase and $\mathbf{S}_{\text{res}} = \frac{1}{2} (\nabla \mathbf{u}' + (\nabla \mathbf{u}')^T)$ is the resolved strain rate tensor. The Laplacian filter employed in this work is based on a fourth-order discretization, which provides a smooth separation between the large-scale flow structures and the resolved fluctuating components.

The last sink term on the right-hand side of the momentum equation (Eq. (2)) represents the momentum transfer between the continuous and the dispersed phase. In these equations, the volume fraction of the continuous phase is calculated as:

$$\phi_c = 1 - \frac{\sum_{i=1}^n V_i}{V_{\text{cell}}} \quad (7)$$

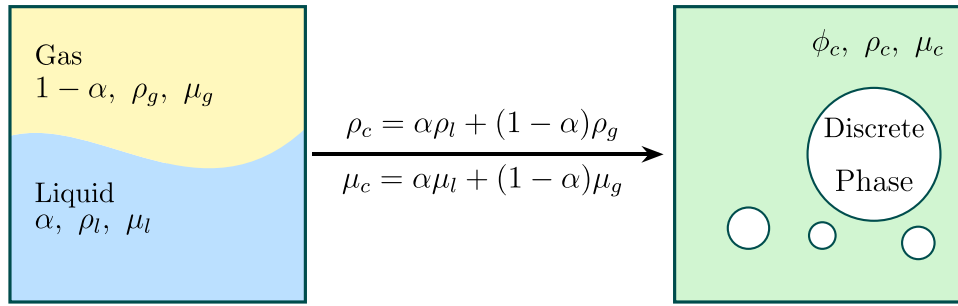


Fig. 1. Schematic view of the Euler-Lagrange coupled with the VOF method.

where V_i is the volume of the i th bubble residing in a cell having the volume of V_{cell} .

As mentioned earlier, the VOF method is only used for the continuous phase, which can consist of two or more phases in a grid cell (e.g. air and water). The free surface can be detected by solving the VOF equation:

$$\frac{\partial \alpha}{\partial t} + \nabla \cdot (\alpha \mathbf{u}) = 0 \quad (8)$$

which is eventually used to determine the properties of the continuous phase as the arithmetic mean of the different phases, such as $\rho_c = \alpha \rho_l + (1 - \alpha) \rho_g$ and $\mu_c = \alpha \mu_l + (1 - \alpha) \mu_g$.

A schematic view of the phase fractions is presented in Fig. 1.

This way, when the dispersed phase enters the grid cell, the volume fraction for the discrete phase coupling is calculated based on the combined continuous phase volume and the dispersed phase volume (Eq. (7)).

It is worth mentioning once again that the VOF method is only used to have a liquid free surface at the top of the plume to prevent any unphysical artifacts that might happen at the upper boundary condition, i.e. when bubbles leave the domain, they drag the liquid outside of the domain with themselves due to the four-way coupling. The solver, in return, re-injects liquid from the top to preserve the total liquid mass in the system.

2.2. Discrete element method

In the DEM method, bubbles are tracked in a Lagrangian reference frame, and the Newtonian equation of motion is solved for every single bubble present in the simulation:

$$m_i \frac{d\mathbf{v}_i}{dt} = \sum_j (\mathbf{F}_{ij}^N + \mathbf{F}_{ij}^T) + \mathbf{F}_i^{f-d} + m_i \mathbf{g} \quad (9)$$

Here, m denotes the bubble mass, \mathbf{v} is the velocity, and \mathbf{F}_i^{f-d} is the sum of all the forces exerted on the bubble by the liquid. This includes the drag force, the virtual mass force, and the lift force. The first and last terms denote the collision forces between bubbles and the gravity force. In the conventional discrete element method, the collision forces are modeled using the classic spring-dashpot model. For the case of bubbles, the collision forces are not as large as those of solid materials, and many researchers have ignored this term in their simulations, but recent works have shown that a minimal contact force is required to prevent unphysical overlapping of the bubbles (Xue et al., 2017; Subburaj et al., 2023). In this study, we have used the coefficients provided by Xue et al. (2017).

The drag force imposed on the bubble by the liquid, can be calculated by the following formulation:

$$\mathbf{F}_D = -\frac{1}{2} C_D \rho_l \pi R_b^2 |\mathbf{v} - \mathbf{u}| (\mathbf{v} - \mathbf{u}) \quad (10)$$

Here, ρ_l is the liquid density, and R_b is the bubble radius. The drag coefficient, C_D , used in here is the model provided by Tomiyama et al. (1998):

$$C_D = \max \left[\min \left\{ \frac{16}{Re} (1 + 0.15 Re^{0.687}), \frac{48}{Re} \right\}, \frac{8}{3} \frac{Eo}{Eo + 4} \right] \quad (11)$$

In this equation, the bubble Reynolds number, Re , is calculated as $Re = \nu d_b / \nu$, where D_b is the bubble diameter, and ν is the kinematic viscosity of the liquid. Also, Eo is the bubble Eotvos number calculated as $Eo = g(\rho_l - \rho_b) d_b^2 / \sigma$ in which ρ_b is the bubble density, d_b is the spherical equivalent diameter of the bubble, and σ is the surface tension coefficient.

Virtual mass force in multiphase flows is the body of fluid which the particle displaces with itself when moving through the media (Clift et al., 1978). In the case of bubbles rising in liquid media, the virtual mass force is of great importance, since the density of the liquid media surrounding the bubble is much higher than the bubble itself. Therefore, the virtual mass force interface force model should be considered in the Euler-Lagrange simulation. The virtual mass force can be calculated using the following equation:

$$\mathbf{F}_{VM} = -C_{VM} \rho_l V_b \left(\frac{D_b \mathbf{v}}{D_b t} - \frac{D_b \mathbf{u}}{D_b t} \right) \quad (12)$$

In this equation, D_b and C_{VM} are the bubble diameter, and the virtual mass force coefficient, respectively. The virtual mass force coefficient for a spherical bubble is isotropic and has the value of 0.5. When the bubble deforms from an ideal spherical shape to an arbitrary ellipsoidal shape, virtual mass force tensor is not isotropic anymore, and would have different values in different directions (Tomiyama, 2004; Lamb, 1924). Nevertheless, Zhang et al. (2006) concluded that the value of C_{VM} has minimal effect in Euler-Lagrange simulations of bubble plumes. Therefore, for simplicity, the value of 0.5 was used in this study.

The lift force imposed on a bubble rising in a liquid media can be calculated by the following equation (Auton, 1987):

$$\mathbf{F}_L = -C_L \rho_l V_b (\mathbf{v} - \mathbf{u}) \times (\nabla \times \mathbf{u}) \quad (13)$$

From this equation, it is evident that the lift force acting on a bubble is a result of bubble slip velocity, and the vorticity of the background flow i.e. $\boldsymbol{\omega} = \nabla \times \mathbf{u}$. Similar to every other force model discussed so far, the lift force also needs a lift coefficient, C_L , to close this interfacial force model.

All simulations were performed using the open-source CFD framework OpenFOAM with the MPPICInterFoam solver. This solver provides an Euler-Lagrange formulation in which the continuous phases are resolved in an Eulerian framework using a VOF approach, while the dispersed bubbles are tracked in a Lagrangian reference frame and coupled to the flow through interfacial momentum exchange forces. The dispersed phase is modeled using the Multiphase Particle-in-Cell (MPPIC) method. Although MPPIC is commonly employed in a parcel-based formulation where each parcel represents many physical particles, no coarse-graining was applied in the present study. Each Lagrangian parcel corresponds to a single physical bubble, ensuring a one-to-one representation of the dispersed phase. Unlike classical CFD-DEM approaches that explicitly resolve contact forces through deterministic collision models, MPPIC accounts for bubble-bubble interactions using a stress-based formulation that represents the averaged effect of

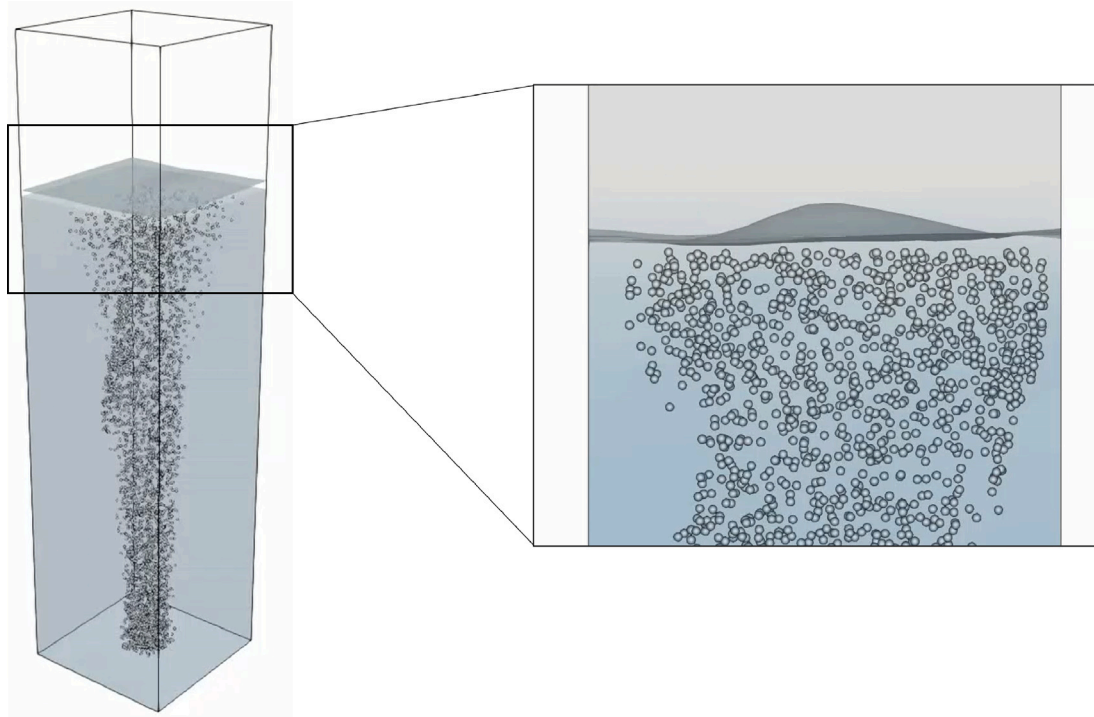


Fig. 2. An instantaneous snapshot of the solver in action, showing the Lagrangian air bubbles and the air/water free surface. The bubble size here is 4 mm, and the superficial gas velocity is 0.49 cm/s.

collisions and crowding. The collision model adopted in this study is formulated as follows:

$$\mathbf{a}_{\text{coll}} = -\frac{1}{\rho_d} \nabla p_d(\phi_d) \quad (14)$$

$$p_d(\phi_d) = \frac{p_0 \phi_d^\gamma}{\max(\phi_{\text{max}} - \phi_d, \epsilon(1 - \phi_d))} \quad (15)$$

In Eqs. (14) and (15), \mathbf{a}_{coll} denotes the acceleration term representing the collective effect of bubble–bubble interactions in the MPPIC framework, ρ_d is the density of the dispersed phase, and ϕ_d is the local dispersed-phase volume fraction. The function $p_d(\phi_d)$ is the particle-phase pressure that accounts for collision and crowding effects through a continuum stress formulation. Here, ϕ_{max} is the maximum packing volume fraction, p_0 is a scaling constant controlling the magnitude of the particle stress, γ determines the stiffness of the pressure response, and ϵ is a small regularization parameter preventing numerical singularity. In the present simulations, the values $\phi_{\text{max}} = 0.9$, $p_0 = 10.0$, $\gamma = 7.0$, and $\epsilon = 10^{-2}$ were used. As $\phi_d \rightarrow \phi_{\text{max}}$, p_d increases rapidly, generating a strong repulsive stress that enforces volume exclusion in dense regions of the flow.

In this work, this treatment is used primarily to prevent unphysical overlap between bubbles while maintaining numerical stability. Other researchers have used this solver for modeling three-phase gas–liquid–solid flows where the solid stress tensor is an important factor for resolving the flow correctly (Fatehifar et al., 2023; Shang and Liu, 2017). A showcase of the solver in-action for the current application is demonstrated in Fig. 2, where the Lagrangian bubbles and the liquid free surface are captured using the present Euler–Lagrange solver. For further information regarding the use of MPPIC solver, the reader is referred to Henríquez-Vargas et al. (2024).

3. Development of the new lift model

3.1. Physical background on plume hydrodynamics

The presence of the lift force influences the hydrodynamic characteristics of the bubble plume. The lift force essentially influences

the lateral distributions of the bubbles in the plume. In general, for small bubbles rising in a shear flow, the lift coefficient, C_L has positive values, which means the lift force imposed on these bubbles is directed towards the regions of the flow with lower background velocity. On the other hand, larger bubble sizes possess negative values of C_L , meaning the lift force imposed on them is directed towards the regions with higher background velocity. This indicates that for a bubbly plume setting, in which higher velocity regions are near the core of the plume, smaller bubbles tend to spread towards the walls of the column, while larger bubbles tend to accumulate towards the center. This lateral distribution, in turn, affects distinct characteristics and overall flow behavior of the column; thus, the correct definition of the lift coefficient is crucial in bubble plume simulations. One of the most popular lift models in the literature is the model provided by Tomiyama et al. (2002). The formulation of this model is as follows:

$$C_L = \begin{cases} \min[0.288 \tanh(0.121 Re), f(Eo_d)] & Eo_d < 4 \\ f(Eo_d) & 4 < Eo_d < 10 \\ -0.27 & Eo_d > 10 \end{cases} \quad (16)$$

$$f(Eo_d) = 0.00105 Eo_d^3 - 0.0159 Eo_d^2 - 0.0204 Eo_d + 0.474. \quad (17)$$

$$Eo_d = \frac{g(\rho_\ell - \rho_g)d_h^2}{\sigma}. \quad (18)$$

$$d_h = d_b \sqrt[3]{1 + 0.163 Eo_d^{0.757}} \quad (19)$$

This model is mainly a function of the bubble Eotvos number, and the value of the lift coefficient, C_L , drops from positive to negative with increasing bubble size, and for bubbles having Eotvos values of 4 and above, this C_L model will become a function of Eotvos number only. This means that in the Tomiyama lift model for a mono-dispersed bubble size system, the value of C_L is the same for all of the bubbles.

In the past few years, researchers have discovered that the value of the lift coefficient changes based on various flow-related characteristics. An example of these recent discoveries could be the lift coefficient modeling provided in the work of Hessenkemper et al.

(2021). This model was published more recently and does not assume a constant value for the lift coefficient. Instead, the C_L value changes not only based on the bubble size, but also in response to the local flow properties, and reads $C_L = f(Sr, Re) - f(Eo_{\perp})$. This model consists of two essential parts. The first part, $f(Sr, Re)$, relates to the local dimensionless shear rate (Sr) and Reynolds number (Re), and was deduced in the work of Legendre and Magnaudet (1998). The second part, $f(Eo_{\perp})$, includes the effect of bubble size and deformation using the modified Eotvos number. The complete definition of the parameters used in this model is given below:

$$f(Sr, Re) = \left[\left(\frac{6}{\pi^2} \frac{1}{\sqrt{Re} Sr} - \frac{2.255}{(1 + 0.2 \epsilon^{-2})^{3/2}} \right)^2 + \left(0.5 \frac{Re + 16}{Re + 29} \right)^2 \right]^{1/2}, \quad (20)$$

$$Re = \frac{\rho_L u_{\text{slip}} d_B}{\mu}, \quad Sr = \frac{d_B v}{u_{\text{slip}}}, \quad \epsilon = \left(\frac{Sr}{Re} \right)^{1/2}, \quad (21)$$

$$f(Eo_{\perp}) = \frac{\ln(1 + \exp(-12G))}{12}, \quad (22)$$

$$G = \frac{0.11 \ln(1 + \exp(4(Eo_{\perp} - 5.6)))}{4} - 0.14(Eo_{\perp} - 5.2) - 0.44. \quad (23)$$

$$Eo_{\perp} = \frac{g(\rho_{\ell} - \rho_g) d_h^2}{\sigma}. \quad (24)$$

$$d_h = d_b \sqrt[3]{1 + 0.65 Eo^{0.35}} \quad (25)$$

A complete list of the most important bubble lift force models available in the literature is provided in the work of Subburaj et al. (2023). Nonetheless, most of the existing C_L models used in Euler–Lagrange simulations show discrepancies with experiments, which stems from the fact that many of these models were derived using experiments of single bubble measurements, and these experiments were usually conducted in a laminar or stratified liquid medium. However, the hydrodynamics of a bubbly plume is different compared to single bubble setups, or even single-phase plumes. Li et al. (2020) conducted a systematic experimental comparison between single-phase and bubbly plumes. By keeping the fluid inlet flow constant, they compared the hydrodynamics of single-phase plumes, small-bubble dense plumes, and large-bubble dilute plumes. The comparisons elucidated that plumes that are generated by small bubbles, ranging between 2 to 3 mm, behave similarly to plumes generated by liquid injection into the media, even though the momentum flux in the bubbly plume is higher than that of single-phase plumes due to the presence of the bubbles. The hydrodynamics of these plumes is mainly characterized by the linear spreading of the plume width and decreasing of the centerline velocity with height, indicating that the positive lift force imposed on these bubbles stays almost constant throughout the rise path. When the bubble plume comprises larger bubbles (5 to 6 mm), the hydrodynamics change drastically. For the same flow-rate, liquid entrainment and plume-induced shear is higher and that is due to stronger wake turbulence introduced to the liquid. The plume width does not increase with height anymore and is narrower compared to the small-bubble plume. This corresponds to the negative value of C_L for large bubbles. However, with a higher gas flow rate, the plume becomes wider, and the bubbles disperse more, which seems contradictory to the established understanding of the lift force imposed on large bubbles based on single bubble studies.

The turbulent characteristics of plumes are a defining factor in their behavior. Plumes containing larger bubbles show strong anisotropy in turbulence (Wu et al., 2021; Huang et al., 2025). Velocity fluctuations in the vertical direction are generally larger than in the horizontal direction because of the higher rise velocity of the bubbles and strong vertical wakes generated by the bubbles. As a result, the momentum amplification factor in the vertical direction is stronger than in the

horizontal directions (Fraga and Stoesser, 2016). These anisotropic characteristics of turbulence, and higher momentum amplification in the vertical direction, lead to the bubbles following the vertical buoyant path of the plume more rather than spreading laterally. These wakes also actuate turbulent energy decay and increase the turbulent dissipation rate, ϵ . In the work of Wu et al. (2021) it was shown that ϵ has high peak values towards the center line, almost an order of magnitude larger than in the small bubble case. High values of ϵ cause plume spreading to increase by dissipating the turbulence in the lateral directions. Turbulence dissipation also hinders the amplification of momentum in the vertical direction due to the faster decay of the vertical momentum and turbulent velocity fluctuations. This means that for large bubble/low flow-rate plumes ($Q_G = 0.25$ L/min in the work of Wu et al., 2021), the plume spreading is limited, corresponding to negative values for C_L . However, in higher flow rates ($Q_G = 1.2$ L/min), extremely high dissipation rates arising from the strong turbulence generated by larger bubbles cause the plume to spread more than in the lower flow-rate case.

In the work of Kulkarni (2008), the lift coefficient of bubbles rising in a plume was examined for the first time using experiments. In this work, bubble sizes in the range of 2 to 6.5 mm were studied, which covered the onset of lift force reversal reported by Tomiyama et al. (2002). Here, it was observed that turbulent kinetic energy (TKE) causes the bubbles to travel towards the center of the plume, and higher values of TKE correspond to higher values of negative C_L . They also noticed that in the turbulent regime of the plume, the reversal of lift force towards negative values happens in smaller bubble sizes around 4.7 mm compared to what was noticed in single bubble experiments of Tomiyama et al. (2002) which were rising in a viscous liquid where turbulence effects were absent. This trend was also observed in later studies of bubbles rising in water (Hessenkemper et al., 2021; Hayashi et al., 2021). They also reported that turbulent dispersion acts in opposition to the lift force and promotes outward bubble motion. They proposed a lift coefficient model based on the instantaneous and local TKE, and they plotted the C_L values for their plume, which shows that C_L values change radially and axially. This indicates that C_L changes drastically in the dynamic turbulent flow of the plume. Nonetheless, this model neglects other important mechanisms which directly influence the lift force, such as shear rate, Sr , and turbulent dissipation rate ϵ .

Throughout all of the research papers published on the lift force phenomenon, shear rate and vorticity are consistently identified as two of the most influential flow properties governing the lift force emergence. The high shear rate affects the lift force in two ways: first, it leads to higher exposure of the bubble to the vorticity in the background flow, and second, it causes more deformation of the bubble shape, which in turn results in more vorticity generation at the bubble surface. Legendre and Magnaudet (1998) reported that in high Reynolds numbers, such as air/water bubbly flows, an increase in Sr causes the values of C_L to decrease. They reported that shear rate influences the bubble lift force through vorticity generation near the bubble. Sankaranarayanan and Sundaresan (2002) also reported a similar dependence of C_L on Sr , but in a bubbly plume setting. In addition, researchers have found that the lift reversal of the bubbles is due to higher vorticity generation at the bubble surface. A comprehensive review of the current understanding of bubble vorticity generation can be found in our previous study (Zand et al., 2025).

3.2. Theoretical basis of the new lift model

In order to develop a C_L model based on turbulent kinetic energy, turbulent dissipation rate, and vorticity, the trends and profiles of these flow characteristics must be studied in a plume. We initiate our investigation on single-phase plumes to obtain an analytical grasp of the physics of these flows, with turbulent kinetic energy k , ϵ , and ω being the focal point of the observations specifically. Afterwards,

the analyses are extended to multiphase bubbly plumes. As mentioned in the previous section, the turbulence is anisotropic and momentum amplification is larger in the vertical direction along the rise path of the plume. In this regime, turbulent eddies drag the flow along the rise path. This results in coherency of the plume in strong turbulence, and keeps the flow from dispersing in the lateral direction.

In turbulence physics, one of the characteristics time scales is the eddy turnover time which can be defined proportional to the ratio of k and ϵ . This time scale indicates the amount of time a turbulent eddy is able to keep its kinetic energy before transferring to smaller scales. In the context of turbulence modeling, it is also used as the turbulence decay time scale (Karimpour and Venayagamoorthy, 2013) that reads

$$\tau_e = C_\tau \frac{k}{\epsilon} \quad (26)$$

with C_τ being a dimensionless proportionality constant. In fully-developed turbulent jets, higher values of τ_e usually happen further downstream of the nozzle (far-field i.e. $x/d \geq 20$) which is an indicator of the decaying nature of turbulence as expected in the self-preserving region of the jet with dominant dissipation. In this region, turbulent kinetic energy and dissipation rate both decrease with distance from the nozzle, but the rate of decrease of dissipation rate is much faster than kinetic energy, e.g. for circular jets $k \sim (x/d)^{-2}$ and $\epsilon \sim (x/d)^{-4}$ (Antonia et al., 1980). Thus, the turbulent time scale increases with distance from the nozzle as $\tau_e \sim (x/d)^2$. It has to be noted that C_τ could vary depending on the nature of the turbulent flow. For instance, in different numerical simulations of multiphase flows, values in the range of 0.15 to 1 have been approximated (Murman, 2013; Kubilay et al., 2015; Schneiderbauer and Saeedipour, 2019; Saeedipour and Schneiderbauer, 2025).

The other flow quantity that certainly affects the lateral movement of the flow is vorticity. Particularly, in the case of bubbly flows, vorticity is the driving mechanism for the lift force acting on bubbles that contributes to the heterogeneity of the plumes. Following the same strategy for turbulence decay time scale, here we adopt a vorticity-based time scale to describe the local rotation of fluid element:

$$\tau_\omega = \frac{1}{\|\omega\|} \quad (27)$$

This time scale indicates the local persistence of turbulent eddies and has been used in the literature to explain the interaction of vorticity and turbulence (de Wit et al., 2024), or to describe particle clustering in shear-vorticity dominated flows using the particle response time to vorticity (Shi et al., 2022). Thus, unlike τ_e , the vorticity-based time scale could be more relevant to describe local phenomena in turbulence, for instance, as a local turnover time (Lesieur, 2008), rather than the global or averaged interpretation of turbulence physics. In the present attempt for the bubble lift model, we assume τ_ω is pertinent in lift generation as it can express the amount of time a Lagrangian bubble is exposed to a vorticity field in its surrounding that generates its lift.

It has to be emphasized that both τ_e and τ_ω represent characteristic time scales that carry information on different aspects of turbulent motions. Different studies have used these time scales from different theoretical standpoints, and have chosen one of them depending on the objectives of the study. However, to our best knowledge, no prior work in the literature has simultaneously investigated both of them or explicitly compared them in one canonical flow configuration, such as homogeneous isotropic turbulence or freely decaying jets. The comparison between these two time scales allows to define a new dimensionless parameter, β , which reads

$$\beta = \frac{\tau_\omega}{\tau_e} \quad (28)$$

In order to give a physical interpretation of this time ratio and illustrate the role of β in the dynamics of the jet, we hypothesize a schematic picture of a submerged single-phase plume (shown in Fig. 3) generated by injecting liquid into a liquid medium. The plume behaves like a coherent jet in the beginning, and as we later show, β

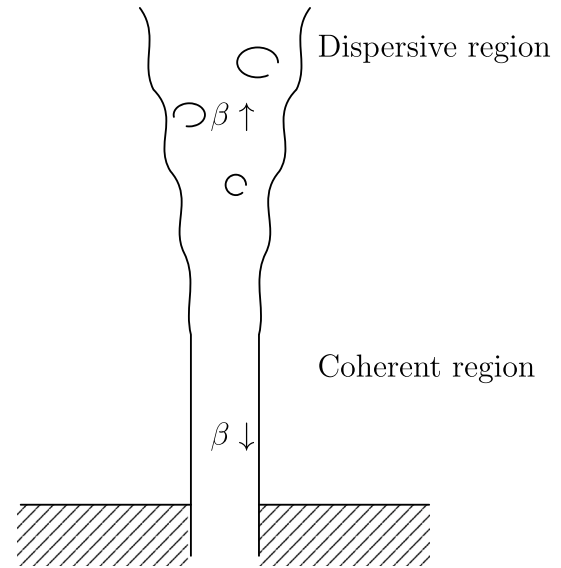


Fig. 3. Schematic of a single-phase plume with a jet-like core and dispersive vortical region downstream. The variation in β is schematically shown based on the time-averaged profile along the central axis of the plume.

is small because the vorticity-based time scale is relatively short, and the turbulence decay time is extremely high due to high production of kinetic energy at the inlet. As discussed before, this turbulent kinetic energy is strongly anisotropic in the vertical direction and carries the flow upwards. After ascending for some time, β increases because the turbulent intensity diminishes with distance from the nozzle, which, in turn, results in larger turbulent structures. Therefore, τ_ω grows as these eddies are of lower vorticity strength compared to the ones closer to the injection point. This insight also implies that the jet becomes more dispersive downstream of the nozzle.

Therefore, we hypothesize that this time ratio reflects the competition between dispersion and coherence of the jet and can be used as the basis for modeling the lateral motion of bubbly plumes. Based on this physical intuition, we relate the bubble lift force model to the behavior of β downstream of the plume. Nevertheless, due to the complexity of the interactions between bubbles and the flow structures in a two-phase system, it is instructive to continue the discussion based on some preliminary simulations.

3.3. Simulation setup

The bubble plumes studied in this paper are two 3D and a pseudo-2D bubble plumes, both of which have rectangular cross sections with different aspect ratios. The 3D bubble columns are simulated based on the experimental data of Deen (2001) which are frequently used in the literature as benchmarks used for validation purposes. There are two columns which have width and depth of 0.15 m, but their difference is the height of the plume, which for the shorter one is 0.45 m and for the taller one, it is 0.9 m. This makes the aspect ratio of the columns $H/W = 3$ and 6, respectively. The schematic view of the bubble plume used in these simulations is presented in Fig. 4. Boundary conditions used for the side walls and the bottom plane (excluding the inlet) are no-slip condition for the continuous phase and rebound for the discrete phase. At the inlet section, a free-slip condition is selected for the liquid. The discrete bubbles are injected through the rectangular inlet patch. At the top plane, a pressure outlet was used for the continuous phase (here, air, since the liquid does not reach the top). At the liquid free surface, bubbles are simply deleted from the simulation to prevent them from entering the air phase as a particulate entity and causing any non-physical accumulation.

Table 1
Details of the cases simulated in this study.

Parameters	3D	Pseudo-2D
	$H/W = 3, 6$	$H/W = 16$
Dimensions	$0.15 \times 0.15 \times 1 \text{ m}^3$	$0.11 \times 0.05 \times 2 \text{ m}^3$
Inlet size	$37.5 \times 37.5 \text{ mm}^2$	$80 \times 20 \text{ mm}^2$
Mesh no.	$15 \times 15 \times 100$	$11 \times 5 \times 120$
Superficial gas velocity, N_b	0.49 cm/s	0.30 cm/s
Liquid free surface, H	0.45 m, 0.9 m	1.8 m
Bubble density, ρ_{bubble}		1 kg/m ³
Fluid density, ρ_f		1000 kg/m ³
Fluid viscosity, μ_f		0.001 Pa s
Time-averaging window		50 s – 500 s

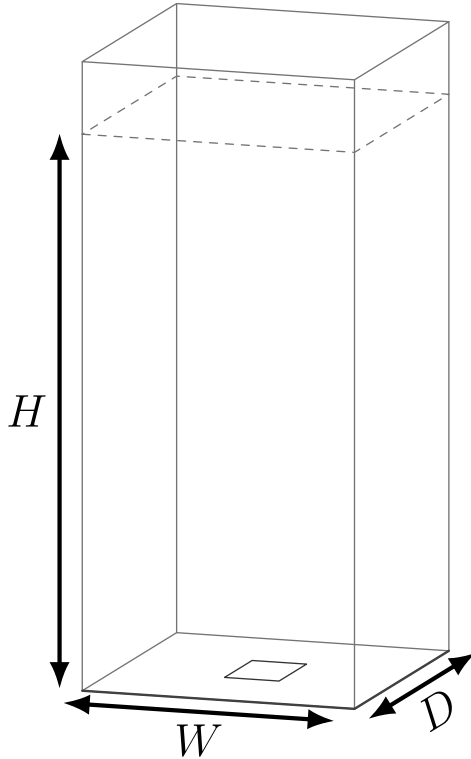


Fig. 4. Schematic view of the rectangular geometry of the bubble plumes used in this study.

According to the reference, the bubbles injected into these systems have a uniform size of 4 mm, and the superficial gas velocity is 4.9 mm/s. The gas is injected into the system through a square inlet with dimensions of $0.0375 \text{ m} \times 0.0375 \text{ m}$, located at the bottom of the device (Deen, 2001). The pseudo-2D bubble plume is based on the experimental work of Lucas and Ziegenhein (2019). The dimensions of this setup are $0.1125 \text{ m} \times 0.05 \text{ m} \times 2 \text{ m}$ ($W \times D \times H$), and the gas inlet in the experimental setup consists of six needles at the bottom of the setup. In the experiments, different nozzle sizes were used to investigate the effect of bubble size on the flow dynamics. In the present study, we have selected the largest bubble sizes reported in their paper, namely, case 6–70 in the paper. Due to the complexity of the inlet arrangement and the mesh requirements of the coupled Euler–Lagrange framework, where the grid size needs to be considerably larger than the bubble size (Esgandari and Schneiderbauer, 2025), a simple inlet plate was used at the bottom of the domain to replicate the gas injection. According to the reference, in this case study, the gas inlet flow is equally distributed between the nozzles, making it a plausible assumption to use a simple patch to inject the gas flow into the domain.

The reported bubble size in this case has a normal distribution with the mean value being around $\mu = 7.12 \text{ mm}$ and the standard deviation being approximately $\sigma = 1 \text{ mm}$. The largest and smallest bubble sizes in this system are 11 mm and 4 mm, respectively. Gas inlet flow-rate was kept constant at 1 L/min in all of the experiments. The large bubbles in this setup are effectively in the negative C_L range according to Tomiyama lift force modeling (Tomiyama et al., 2002), which distinguishes this case from the 3D case. The simulations were run for 500 s. To eliminate the transient effects at the start of the simulation, the first 50 s of the data are excluded from the time-averaged results presented in this work. An overview of the simulation parameters of the cases is presented in Table 1.

To establish a clear hydrodynamic baseline, the first set of simulations considers a single-phase plume that employs the same volumetric inlet flow rate and geometric configuration as the 3D Deen case. The inlet width and resulting aspect ratio $H/W = 6$ are therefore preserved, and the computational setup remains unchanged except that water is injected through the inlet instead of bubbles. This configuration allows the underlying plume dynamics to be examined in isolation, without the additional complexities associated with a dispersed phase, such as introducing the modelings of interfacial momentum transfer mechanisms, such as lift, drag, and virtual mass, as well as bubble-induced modifications of the local turbulence field. The single-phase plume is simulated using a large eddy simulation framework, in which the dominant turbulent motions are resolved explicitly while the unresolved scales are modeled. The analysis of this reference case is conducted in terms of the previously introduced quantities: the eddy turnover time τ_e , the vorticity-based time τ_ω , and their ratio β . By examining the vertical evolution of and the corresponding profiles of β , the plume's dispersion characteristics can be interpreted in relation to the local balance between turbulence timescales and vorticity persistence. This single-phase study thus provides a controlled hydrodynamic reference against which the subsequent bubbly plume simulations may be compared, enabling a clear distinction between dispersion features intrinsic to the carrier phase and those that arise only through the presence of bubbles and their associated interfacial forces.

A grid dependence test was done prior to studying the flow characteristics to check the validity of the single-phase simulations. The initial mesh size of 20 mm was selected, making the mesh number $8 \times 8 \times 50$ in the width, depth and height of the geometry, totaling a number of 3 200 grid cells in the entire domain, which is considered grid size number 1, G1. The mesh size was then reduced multiple times to resolve the flow with smaller grids, yielding grid counts of G2 = 25 600, G3 = 204 800, and G4 = 691 200 cells. By comparing the time-averaged axial velocity profiles at $z = 0.2 \text{ m}$ in Fig. 5, it was concluded that the grid resolution of G3 is accurate enough to resolve the single-phase flow.

An instantaneous snapshot of the jet is presented in Fig. 6(a). From this snapshot, it is evident that the plume shows a coherent structure in regions close to the liquid inlet, and the jet core is confined without much spreading. Higher up in the liquid, the plume starts to disperse in the surrounding media by the generation of vortical structures which carry the flow in the lateral directions. This behavior of the plume can

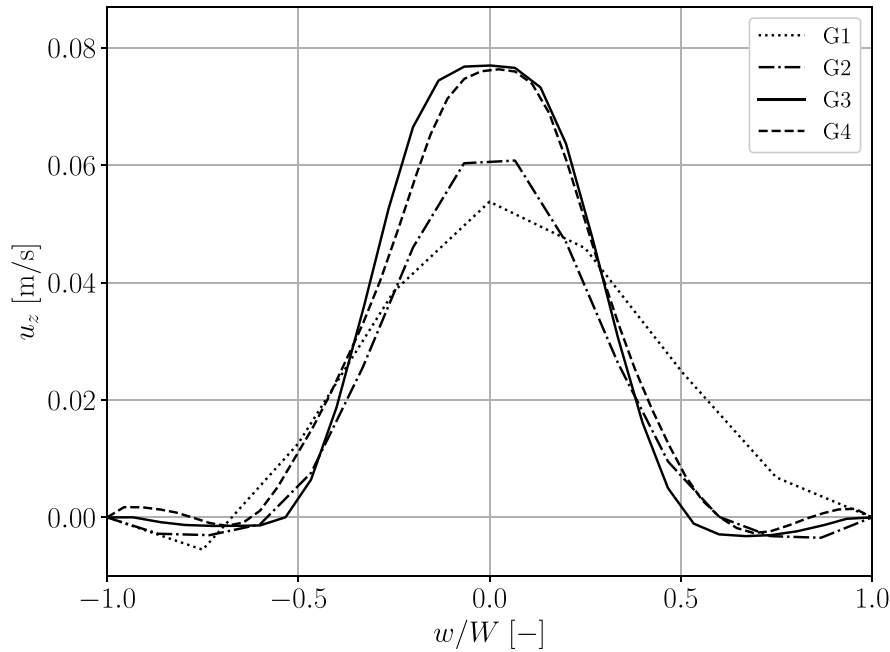


Fig. 5. Grid dependence study of the single-phase jet using the time-averaged axial velocity profiles at $z = 0.2$ m.

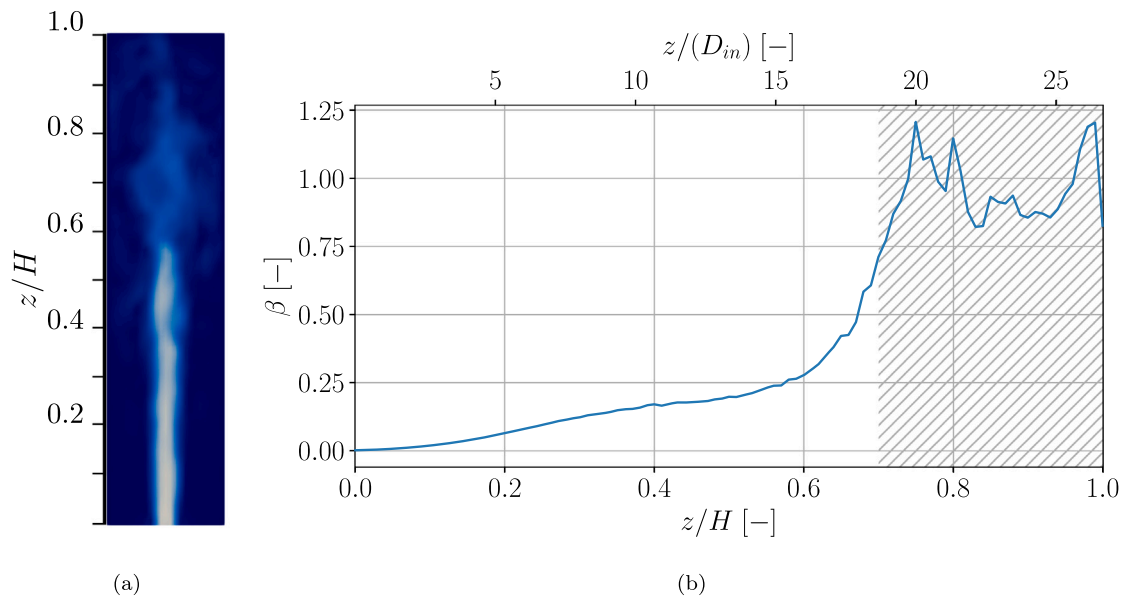


Fig. 6. Single-phase jet: (a) time-averaged velocity contours, (b) time-averaged values of β along with the central axis. The hatched area in the plot denotes the region above the free surface.

be described by looking at the time-averaged β profile along the rise path, which is brought in Fig. 6(b). In this plot it can be seen that β starts from low values in the vicinity of the inlet. By traveling upwards along the axis of the plume, β starts to increase, and this increase corresponds to dispersive behavior of the plume seen in the snapshot (Fig. 6(a)). The hatched region in the plot represents the region of the flow where a plume structure cannot be detected in the flow anymore, and lateral dispersion is strong (higher up in the domain).

For the case of bubbly plume, the hydrodynamics is more complicated. In the work of Subburaj et al. (2023), it was shown that the 3D bubbly plume in both cases of $H/W = 3, 6$ starts to disperse rigorously

at regions closer to the inlet of the gas phase, and the lift coefficient has values closer to or even higher than 0.5, namely the Auton (1987) model. As the plume rises, bubble lateral dispersion becomes less and at the mid section of the taller plume, the Tomiyama et al. (2002) model ($C_L = 0.288$) over-predicts the gas dispersion. Moreover, at the regions closer to the upper section of the taller plume, only C_L values closer to zero or even negative can depict the liquid velocity profiles. This dynamic behavior of the gas bubbles can be described by examining the axial profile of β in Fig. 7.

Time-averaged values of β are plotted along the centerline axis of the plume in Fig. 7. The figure reveals that the presence of bubbles

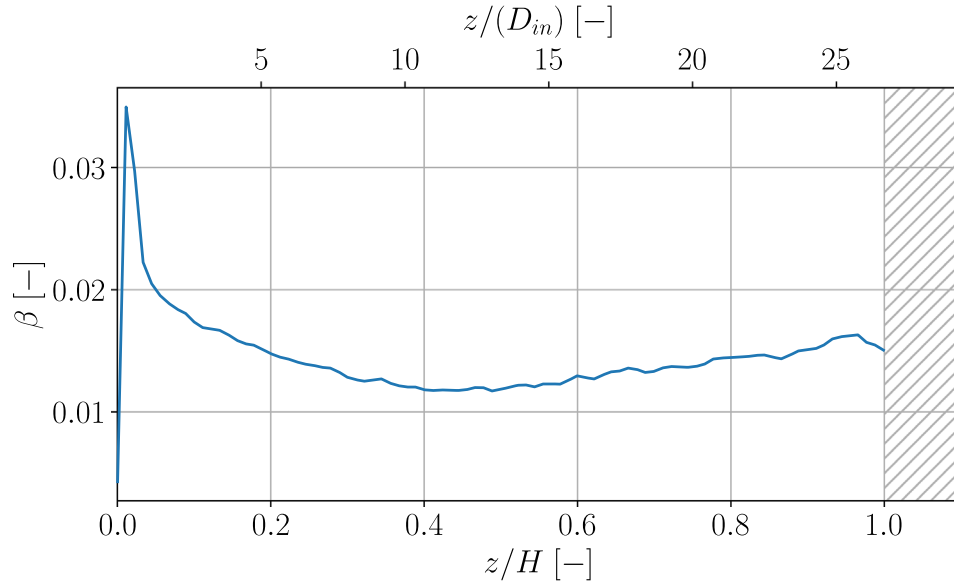


Fig. 7. Time-averaged values of β in the 3D bubbly plume with $H/W = 6$. The hatched area in the plot denotes the region above the free surface.

affects the profile of β compared to single-phase plume. In the regions closer to the gas inlet, β has peak values compared to regions higher in the plume. When moving upwards in the plume, β profile shows a sharp reduction in the beginning, followed by a more gradual reduction towards the mid-section. The profile is almost constant in the middle to mid-high regions, with a mild increase in the regions closer to the surface. This is inline with the observation reported by Subburaj et al. (2023) indicating that the plume spreads in the beginning whereas the spreading stops at some region in the middle of the column.

In spite of having no further validation for the trend of β observed in Fig. 7, we base our new lift model on the behavior of this temporal-scale ratio as hypothesized earlier in sub-Section 3.2. We select the taller 3D column for investigating the relation between bubble C_L and β , since the flow is more dynamic, and covers a wider range of dispersion to coherence regimes. To also account for bubble size in the C_L model, bubble modified Eotvos number Eo_d is also incorporated in the formulation. Since, according to the literature, Eo_d is inversely proportional to C_L , meaning larger bubble sizes tend to have negative values of lift coefficient, Eo_d is incorporated in the denominator of the formula. Another parameter that has been used in the literature to define the lift coefficient models in bubbly flows is the gas volume fraction (Subburaj et al., 2023; Kulkarni, 2008). Volume fraction is generally associated with positive values of C_L , and regions with a higher concentration of bubbles experience more gas dispersion. In this study, by taking a look at the radial profiles of β (not presented here), it was observed that β has extremely high values near the walls of the domain. This will result in high positive values of C_L in the regions near the walls, which in turn causes bubble accumulation in these regions. Gas volume fraction is used in the nominator of the formula to mitigate these peak β values near the walls. The resulting expression to be used in the lift coefficient reads

$$\beta_L = \frac{\tau_\omega}{\tau_e} \cdot \frac{\phi}{Eo_d} \quad (29)$$

Following the strategy of previous research (Tomiya et al., 2002; Subburaj et al., 2023; Kulkarni, 2008), a polynomial function based on β_L was considered to formulate C_L values, which can depict the flow profile of the bubbly plume. Different polynomial functions were tuned to reproduce the liquid velocity profiles reported in the classic experiments of Deen (2001). The experiments conducted by Deen (2001)

represent one of the most well-established reference cases in the literature for several reasons. First, the bubble size considered in this study lies in the transition region between positive and negative lift force emergence. This makes it particularly suitable for understanding the conditions under which the sign change of the lift force occurs, and for assessing whether this transition is governed solely by bubble size and local vorticity, or if other flow properties also play a significant role. Second, the bubble column is operated in a highly dynamic regime, where the flow characteristics vary substantially along the vertical direction, especially in the taller setup. This gave the opportunity to study the influence of the flow properties on the evolution of the lift force in terms of the sign and magnitude change. The coefficients of the polynomial function were determined through a systematic calibration procedure, aimed at reproducing the velocity profiles reported in Deen (2001). The resulting lift coefficient function is given as follows:

$$C_L = \begin{cases} a\beta_L^3 + b\beta_L^2 + c\beta_L + d & \beta_L < 4 \times 10^{-5} \\ 0.55 & \beta_L \geq 4 \times 10^{-5} \end{cases} \quad (30)$$

$$a = 1.282 \times 10^{11}, \quad b = -1.581 \times 10^8, \quad c = 5.178 \times 10^4, \quad d = -1.220$$

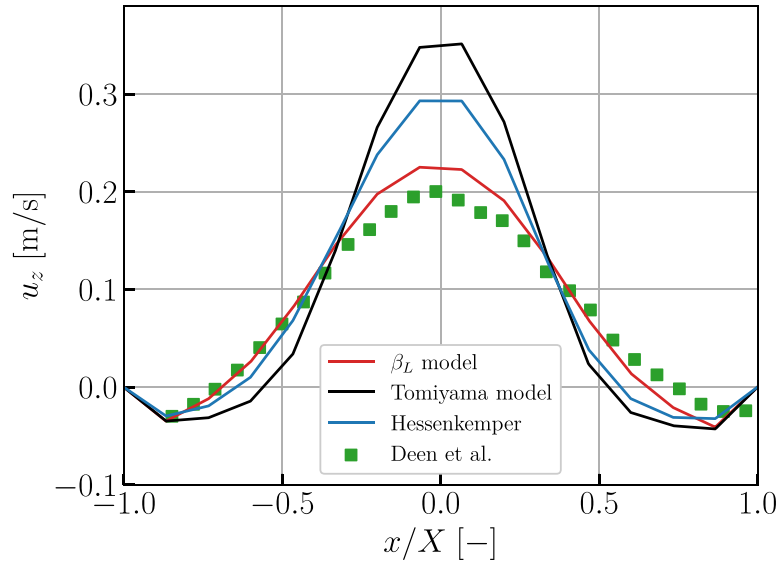
It has to be mentioned that the dimensionless quantity β_L can be evaluated using the parameters in Euler-Lagrange large eddy simulation as the associated time scales can be computed by resolved vorticity, turbulent kinetic energy (Eq. (5)) and dissipation rate (Eq. (6)) in each computational cell, and Eo_d is accessible for each Lagrangian bubble. Therefore, the proposed lift model is practically applicable in the present Euler-Lagrange solver. It remains to analyze the performance of this model in the next section.

4. Results and discussions

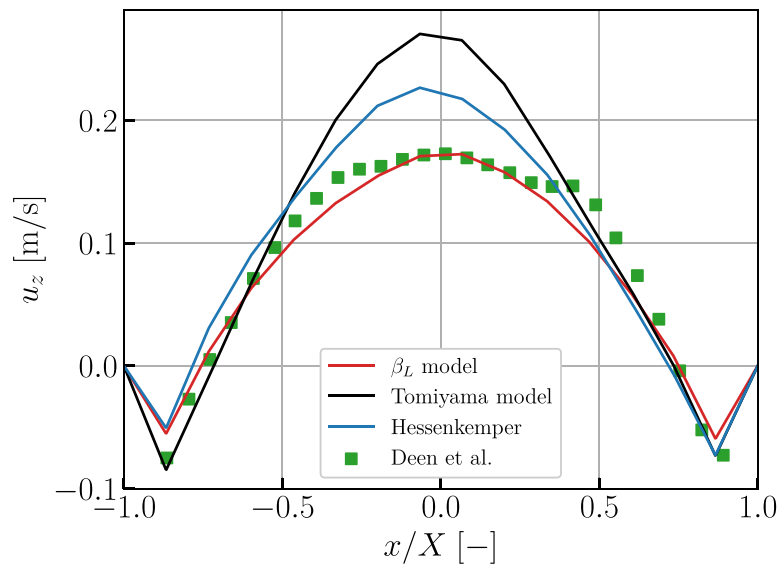
In this section, the accuracy and performance of the proposed model are evaluated against the single-bubble-driven C_L models in depicting a series of experimental data from literature as well as an in-house experiment. These models are used as reference in order to assess the performance of the proposed lift model under identical numerical and physical conditions. In addition to the classical formulation of Tomiya et al. the flow-responsive model of Hessenkemper et al. is also considered, allowing a comparison with both constant and

Table 2
Summary of the experimental benchmarks used for model validation.

Case	Injection profile	Bubble size	Shear rate	Nominal lift	Source
Mono-D4	Mono-disperse	4 mm	$0.2 < Sr < 1.2$	transitional	Deen (2001)
Poly-D7	Poly-disperse	4–11 mm	$1 < Sr < 2$	negative	Lucas and Ziegenhein (2019)
Poly-D2	Poly-disperse	0.5–3 mm	$0 < Sr < 0.3$	positive	in-house experiments



(a) $h = 0.15$ m



(b) $h = 0.35$ m

Fig. 8. Liquid velocity profiles of the Mono-D4 plume with $H/W = 3$ at different heights. The discrete symbols denote experimental data, whereas the curves correspond to simulations using different models.

dynamic single-bubble-based closures. The experimental benchmark cases employed for this comparison are summarized in Table 2, which include configurations with different injection conditions, bubble size distributions, and lift-force regimes, providing a structured basis for the systematic evaluation of the lift models. The typical range of shear rate of the bubbles is also brought in the table to illustrate in which cases the assumption of weak shear conditions which is experienced by single

bubbles rising in a shear flow is no longer valid (Auton, 1987; Legendre and Magnaudet, 1998).

4.1. Case Mono-D4

In the 3D plume cases, the time-averaged liquid velocity profile is reported at different heights of the plume for both taller and shorter

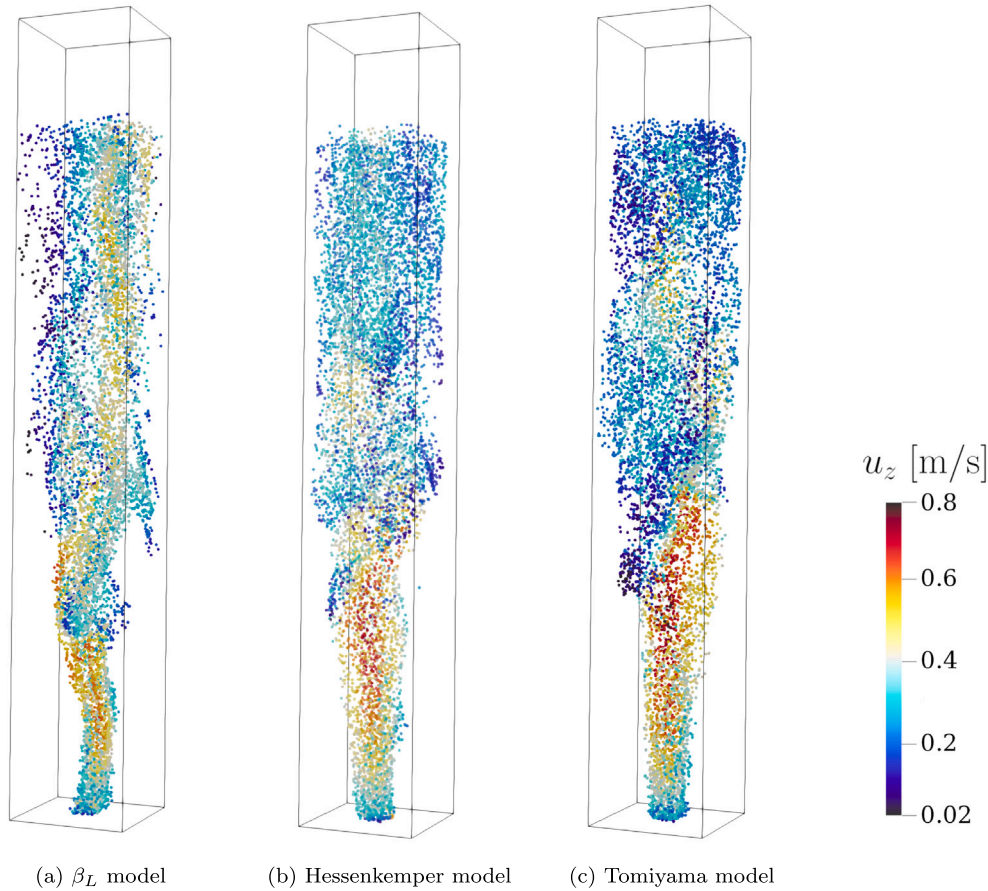


Fig. 9. Instantaneous snapshots of the bubble plumes simulated using different lift force model. The Lagrangian bubbles are colored with their rise velocities. (For interpretation of the references to color in this figure legend, the reader is referred to the web version of this article.)

plumes. First, the results of the shorter column ($H/W = 3$) are compared in Fig. 8. From the velocity profile reported in the experiments, it is evident that the bubble plume has a highly dispersive behavior. Fig. 8(a) shows that the Tomiyama model under-predicts the bubble lift force at the region close to the injection surface, which results in a larger fraction of bubbles rising through the center of the plume and, consequently, a higher velocity profile. Hessenkemper model on the other hand shows a slightly better agreement with the experimental data, as it shows a shorter peak in the middle and a wider distribution of the liquid velocity. This implies that the C_L calculated by this model has larger values. However, this model still over-predicts the liquid axial velocity profile, which means that the C_L of this model is still not large enough to replicate the experiments. The lift coefficient obtained by the β_L model is able to predict the liquid velocity profile accurately at this height of the shorter column. At the upper section of the plume ($h = 0.35$), Fig. 8(b) shows a similar pattern: Tomiyama model yields more deviation from the experimental results, the Hessenkemper model predicts a liquid velocity profile closer to the experimental, and β_L model outperforms the other two models by showing the closest agreement with the experiment. This indicates that although the Hessenkemper model predicts higher C_L values than the Tomiyama model, the resulting lift force still remains insufficient to produce the required dispersed bubble profile. Instead, the proposed β_L model preserves plume dynamics and predicts bubble C_L values more consistent with the experimental observation.

The taller 3D column ($H/W = 6$) has a more dynamic flow behavior, and the lateral distribution of the bubbles follows a more

complicated trend. Fig. 9 demonstrates instantaneous snapshots of the bubbles simulated in the taller Mono-D4 case. With taller liquid height, bubbles undergo various flow regimes. In both the Tomiyama and Hessenkemper models, the majority of the bubbles that have high velocities are in the lower half of the column, and the upper half is crowded with bubbles having smaller velocities. In the β_L model, bubbles forming the core of the plume exhibit relatively high velocities toward the centerline over the entire domain height. This results in a more clearly defined plume core, in contrast to the other two models, where bubbles are more dispersed across the column cross-section. Nevertheless, a decisive conclusion from the bubble motions alone is not possible, since these movements are very chaotic.

The differences between the lift models are clearly reflected in the time-averaged liquid velocity contours shown in Fig. 10. The comparison highlights that the Hessenkemper and Tomiyama models predict significantly higher axial velocities in the lower region of the column, where a narrow and intense high-velocity core is formed close to the gas injection zone. This behavior is in line with the velocity profiles shown later in Fig. 11. However, as the plume rises, the velocity decreases drastically, and the jet-like effect of the plume core is much less pronounced in the upper sections. In contrast, β_L model exhibits a more balanced and consistent velocity distribution along the plume height. Although the axial velocity at the bottom is lower than that predicted by the other two models, the plume retains a coherent high-velocity core as it rises. This results in a velocity field that remains structured and physically consistent throughout the column height, in agreement with the experimental observations formerly discussed.

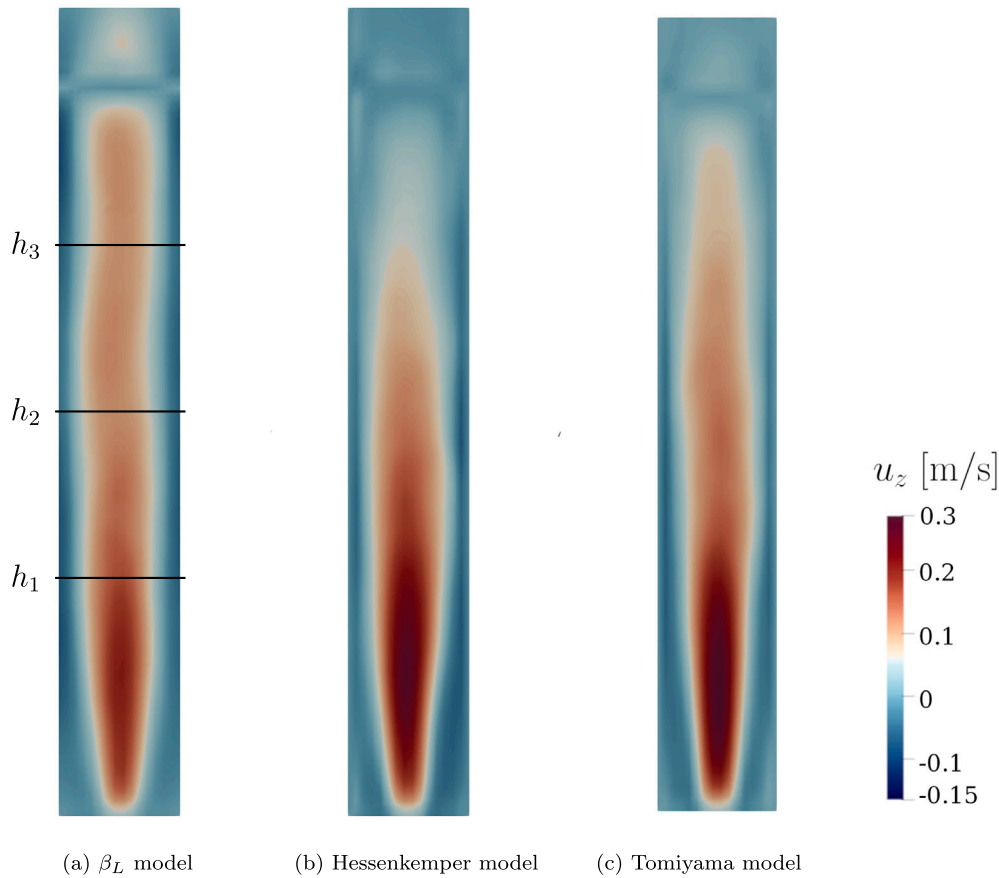


Fig. 10. Time-averaged liquid velocity contours of the Mono-D4 case with $H/W = 6$. The heights at which velocity plots are extracted in Fig. 11 are shown: $h_1 = 0.35$ m, $h_2 = 0.55$ m, $h_3 = 0.75$ m.

In order to have a quantitative analysis of the velocity along the plume height, time-averaged velocity profiles are extracted at different heights (denoted in Fig. 10(a)) and presented in Fig. 11. As shown in Fig. 11(a), both Tomiyama and Hessenkemper models over-predict the liquid velocity profile at the bottom of the plume ($h = 0.35$ m), while the over-prediction by the Hessenkemper model seems to lie in an acceptable range. This demonstrates the relatively strong dispersive behavior of the plume at the bottom, which is captured accurately by the β_L model.

At the middle section of the plume ($h = 0.55$ m), the liquid velocity profile reported by the experiments begins to exceed those predicted by the simulations as shown in Fig. 11(b). At this stage, the plume shows less dispersion and the liquid velocity profile does not show much difference with the lower section. This mitigation of plume dispersion, caused by a decrease in the bubble lift force, is predicted better by the β_L model, while the other two models yield almost similar under-predicted profiles. This increase in the liquid velocity profile is even more pronounced in the upper section of the plume ($h = 0.75$ m), as displayed in Fig. 11(c). Taking into account what is reported in the works of Zhang et al. (2006) and Subburaj et al. (2023), as regards the bubble size keeping a consistent value of 4 mm throughout the whole plume, the value of C_L must have been decreased even more to sustain this high velocity profile. In this section, the models of Hessenkemper and Tomiyama seem to completely fail in capturing the flow dynamics, showing almost flat velocity profiles for the liquid with low values. Nevertheless, the β_L model still shows good agreement with the experimental results even at this height of the plume.

4.2. Case Poly-D7

Next, the simulation results of the pseudo-2D plume in the work of Lucas and Ziegenhein (2019) is discussed. In this work, the time-averaged liquid velocity profile and gas volume fraction measurements are reported at different sections with heights of 600, 1200, and 1600 mm from the bottom plate. The bubble sizes in the experiments (case 6–70) generate a heterogeneous flow regime in the plume, and the velocity profile has peak values towards the center. The velocity profile at the lower section shows a slightly pronounced plateau at the center, which indicates the influence of the arrangement of the injectors, but at the upper sections, the velocity profile shifts completely towards a center-peaked heterogeneous regime. In order to find out which lift models are able to depict this regime change from bottom to top of the plume, three simulations of this plume using the lift models of Tomiyama, Hessenkemper, and the currently proposed β_L model are performed. The accuracy of these models is compared once again for larger bubble sizes and a taller dynamic system. Both the velocity profile and the gas volume fraction, known as gas holdup, are compared with the experiments reported in Lucas and Ziegenhein (2019). The results are shown in Fig. 12.

The experiments show a plateau towards the middle of the system in the lower sections (Fig. 12(a)). This is the region where the flow regime is still influenced by the arrangement of the injection nozzles. Since the bubbles are injected in a uniform manner with respect to the bottom plane, in contrast to the 3D case where the bubbles were injected through the middle of the system, the velocity profile and the

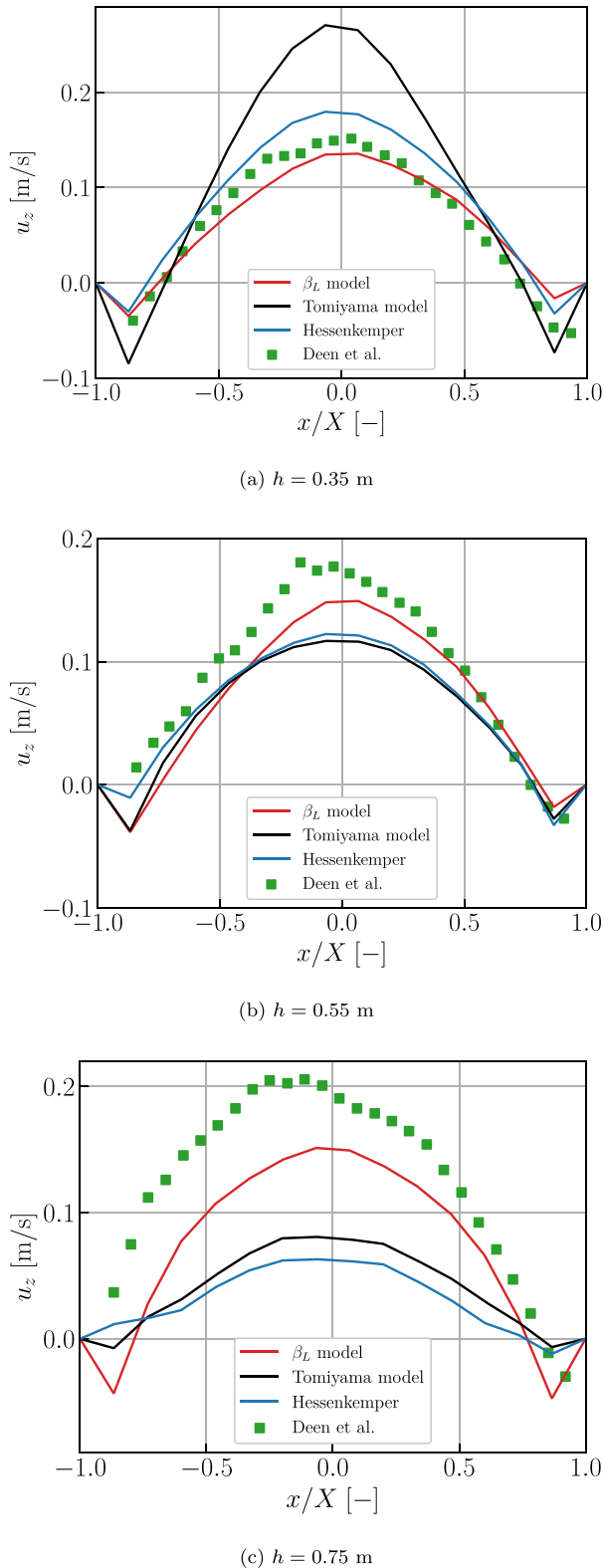


Fig. 11. Liquid velocity profiles of the Mono-D4 case with $H/W = 6$ at different heights. The discrete symbols denote experimental data, whereas the curves correspond to simulations using different models.

gas volume fraction are flatter at the lower sections. In the simulations, this behavior is captured by all three lift models, with the Tomiyama

model having the flattest velocity profile compared to the other models. This implies that the Tomiyama lift model predicts a weaker lift force towards the center in the given system, and therefore, there is a higher distribution of the bubbles to the sides, which entails a lower central peak in the gas holdup profile (Fig. 12(b)). At the mid-section of the plume shown in Fig. 12(c), the plateau is less pronounced, and the velocity profile starts to shift towards higher central peak values. At this stage, the Tomiyama and Hessenkemper lift models start to deviate from the patterns observed in the experiments. In fact, both these models still predict a pronounced plateau in the central region of the domain, indicating that they yield negative values of C_L with small magnitude, which results in an insufficient confinement of the bubble core. On the other hand, the β_L model reveals a stronger peak at the center. The gas holdup profiles in Fig. 12(d) show that the Tomiyama and Hessenkemper lift models predict a double-peak profile near the sides of the domain, whereas the experiments exhibit a single central peak. This transition in the gas holdup profile with increasing height is also correctly captured by the β_L lift model.

Higher up in the column, the flow has fully transitioned to the heterogeneous regime, and both time-averaged profiles of the velocity and bubbles void fraction exhibit a central peak. The profiles demonstrate that at this height, the bubbles are more confined towards the center of the system. While β_L continues to predict this height-dependent transition accurately, the Tomiyama and Hessenkemper models still display flat profiles for both liquid velocity and gas volume fraction. This clearly demonstrates the limitation of these single-bubble-derived models in replicating the regime transition dynamics in the bubble plume.

4.3. Case Poly-D2

Until now, the investigated cases cover bubble sizes in the range of 4 mm and above. In order to test the performance of the proposed lift model for bubble sizes smaller than 4 mm, in-house experiments were conducted to generate a bubbly plume consisting of bubbles smaller than 4 mm. This size range is essential for the closure of the model performance as it encompasses a size range corresponding to positive C_L values.

The test rig consists of a water basin with a square cross-section of $0.5 \times 0.5 \text{ m}^2$ and a water level of 1.5 m (Fig. 13(a)). Bubbles are produced using pressurized air flowing through a cylinder of porous material with 2 cm in diameter. A Bronkhorst air flow controller was used to regulate flow rates from 0 ml/min to 1000 ml/min. The mean diameter of the produced bubbles at a flow rate of 500 ml/min is 1.5 mm. The resulting bubble plume was illuminated with a background LED panel and recorded using a high-speed camera (Photron Fastcam SA3) running at 1 kHz.

A common problem in the processing of bubble plumes is the high number of overlapping bubbles that makes the identification and separation of individual bubbles difficult. Several studies have shown that machine learning techniques can significantly improve bubble segmentation at high overlap rates (Hessenkemper et al., 2022, 2024; Homan and Deen, 2024; Küçük et al., 2026). In the present work we applied the package StarDist (Schmidt et al., 2018, Weigert et al., 2020; Weigert and Schmidt, 2022) for bubble segmentation and the code BlobTracking.jl for Lagrangian tracking of the identified bubble midpoints. The major steps of image processing are briefly described here. Since StarDist is a generic tool it needs a minimum amount of labeled data for transfer learning to adopt to a specific use case. To train the model for our setup, frames well-separated in time were labeled manually with the image processing suite FIJI, and its add-on Labkit. The machine learning model of StarDist then calculates a confidence value for every single pixel indicating a likelihood that this pixel is related to an object representing a bubble. It also generates a set of radii equally spaced in angle to parametrize the shape of the bubble. Since this procedure is repeated for every pixel, all pixels belonging

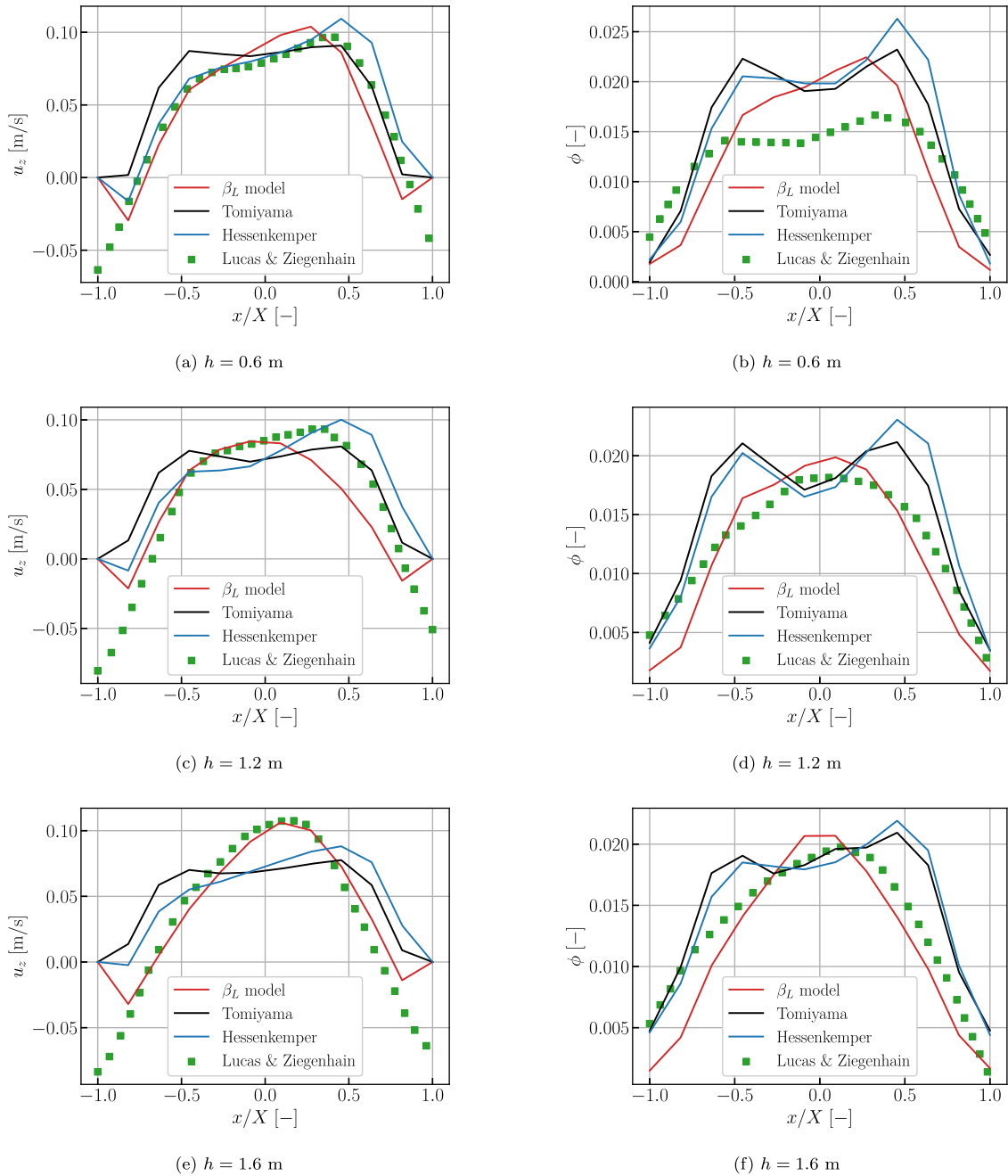


Fig. 12. Time-averaged profiles of Poly-D7 plume with $H/W = 16$ at different heights: liquid velocity (left), and gas holdup (right). The discrete symbols denote experimental data, whereas the curves correspond to simulations using different models.

to the same bubble will result in a similar or identical bubble object. The *non-maximum suppression step* chooses from all neighboring shapes with a high likelihood of approximating the same bubble the one with the highest confidence score. The coordinates of the center of gravity are then exported for tracking of the bubbles across multiple frames (Fig. 13(b)). The way StarDist describes objects by radial rays starting at the center of gravity would, in general, allow to reconstruct overlapping bubbles with high accuracy. Unfortunately, the required format of training data in StarDist does not allow for overlapping labels, which limits this capability to some degree during the training process. Manual checking of the results showed that bubbles are still reconstructed in an acceptable way for small overlaps (10%–20%). We found 16% of bubbles to have an overlap larger than 15% of their area,

which will result in some bias in the statistical bubble size distribution. To overcome this problem, Hessenkemper et al. (2022) implemented an extension to StarDist that corrects the radial rays in overlapping areas. In the present study, however, we only make use of the calculated velocity data derived from the bubble trajectories for the comparison with numerical results, and do not consider such an extension of StarDist. Due to the small timestep of 1 ms between frames, the (2D) distance that the bubble travels is small compared to the distances between neighboring bubbles. This leads to good tracking results, yielding trace data of every bubble, only interrupted if a bubble rises behind another and is obscured to the camera (Fig. 13(c)). Overlapping bubbles will therefore stop the calculation of individual trajectories and consequently eliminate the error in the velocity statistics introduced

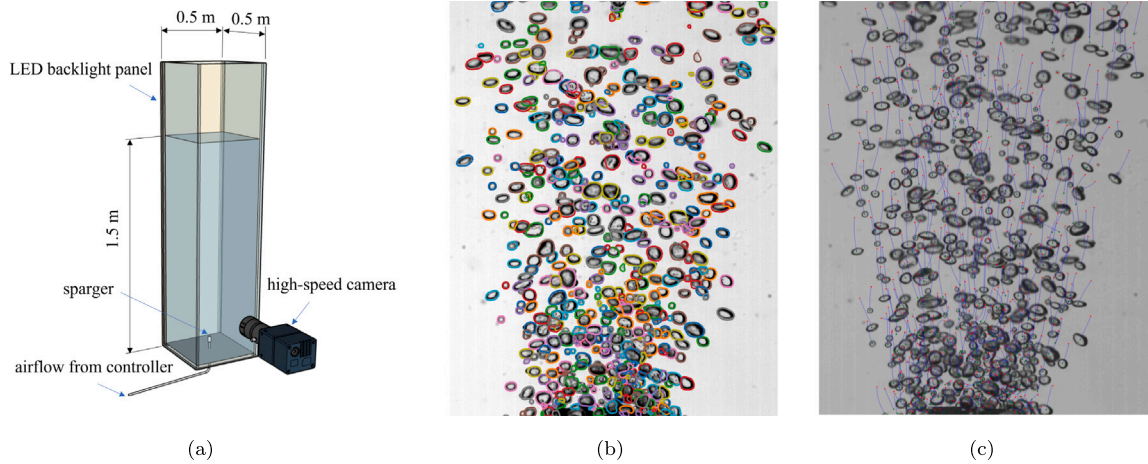


Fig. 13. (a) Setup of the in-house experiment, (b) rendering of star-convex polygons after non-maximum suppression step and (c) visualization of recovered bubble tracks.

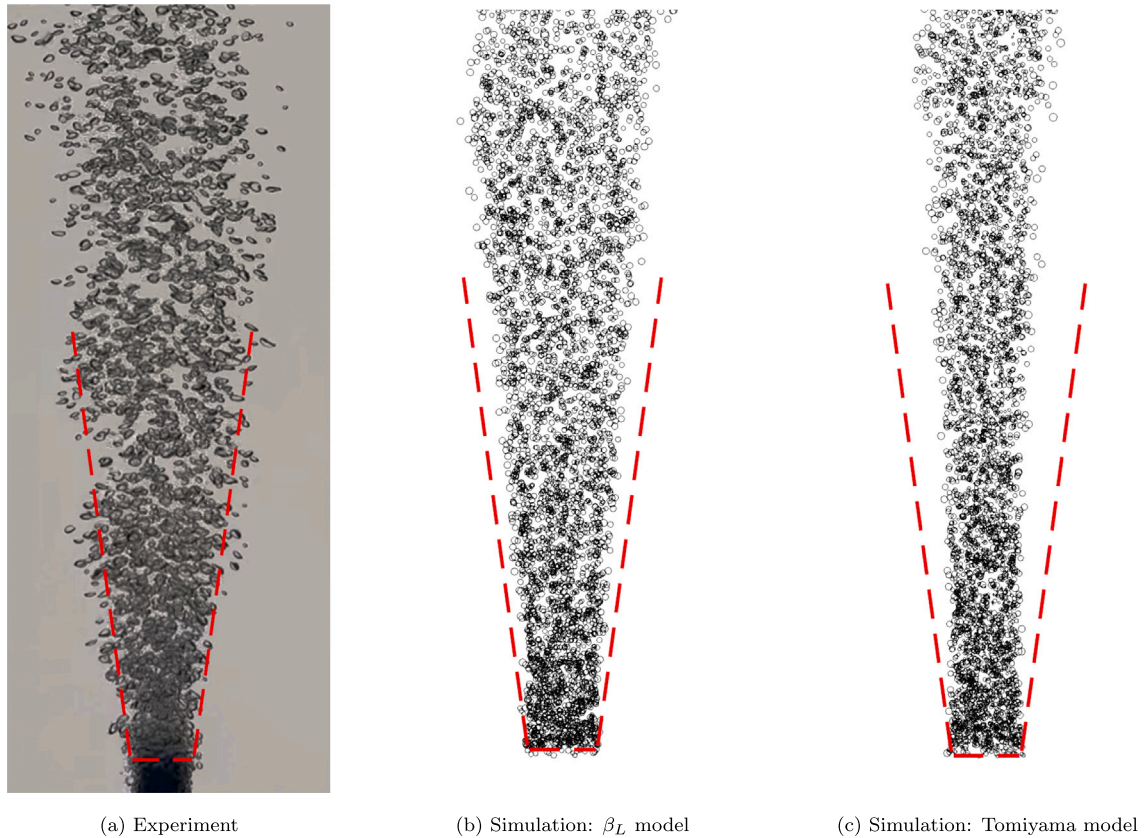


Fig. 14. Instantaneous snapshots of the rising bubble plume in experiment and simulations. The red margins show the expansion angle of the plume in the experiments, which is applied consistently to the simulation snapshots for comparison. (For interpretation of the references to color in this figure legend, the reader is referred to the web version of this article.)

by imperfect reconstruction of overlapping bubbles. Furthermore, the calculation of lateral velocities is not based on consecutive frames but across a minimum time span Δt as explained later on. Hence, only long enough trajectories with a minimum lifetime Δt will contribute to the results.

First, a qualitative comparison of the simulation results using the Tomiyama model and the currently proposed β_L model with the experiments is provided in Fig. 14. This provides a clear visual assessment of model performance in terms of the global plume shape and lateral spreading.

In the experimental snapshot (Fig. 14(a)), the plume width increases gradually with height, indicating a continuous transversal migration of bubbles during their upward motion. A similar trend is observed in the results of the β_L model (Fig. 14(b)), where the plume envelope follows a comparable opening angle and the lateral expansion of the bubble cloud is maintained along the column. In contrast, the Tomiyama model (Fig. 14(c)) predicts a significantly more confined plume, characterized by a narrower bubble core and a reduced spreading rate. The comparison shows that the lateral development of the plume is strongly affected by the lift formulation, and that different lift models lead to

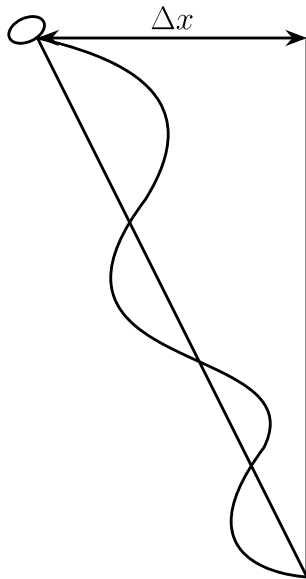


Fig. 15. Schematic representation of bubble total transversal displacement used for calculating transversal velocity.

substantially different macroscopic plume geometries. This qualitative observation provides a first indication of the impact of the lift force on bubble transversal motion and motivates a more detailed quantitative analysis of bubble velocity statistics.

With the Lagrangian data acquired from the image processing and also from the Euler–Lagrange simulations, it is possible to produce the probability distribution function (PDF) of the bubble velocities. As mentioned earlier, the 1000 fps frame rate of the camera used in these experiments provides a high temporal resolution of data acquisition. With this high temporal resolution, the lateral oscillations of the bubbles are captured. The raw lateral velocities computed from the bubble centroids include not only the transverse migration velocities but also the zigzag motion of the bubbles. According to the literature, the magnitude of the horizontal component of bubble oscillatory velocities is in the order of bubble terminal velocity (Mougin and Magnaudet, 2006), which are much higher than transverse migrational bubble velocities due to shear-induced lift force. Since the zigzag motion of bubbles is not resolved in Euler–Lagrange simulations, a direct comparison of the bubble lateral velocity PDFs is not feasible, as these motions differ fundamentally from those observed in experiment. However, bubble rise velocity is less influenced by bubble oscillation, and therefore, the velocities obtained from image processing provide a suitable basis for comparison with the ones extracted from simulations.

For the horizontal component of the velocities, bubbles were tracked for a minimum amount of distance, and the total lateral displacement divided by the total amount of time, Δt , required for this displacement was calculated to figure out the transverse migrational velocity of the bubbles. The Δt used for lateral velocity calculation is 0.1 s, and a schematic representation of the bubble transversal displacement is shown in Fig. 15. Afterwards, in Fig. 16, the PDFs of the Lagrangian bubble velocities are compared with the PDF of velocities extracted from the simulation.

Fig. 16(a) reveals a reasonable agreement between the rise velocity PDFs obtained from experiments and simulation. The simulations reproduce the general PDF shapes and peak locations with good agreement. This indicates that the Euler–Lagrange framework employed in this study is capable of reproducing the dominant vertical dynamics of the bubbles. The small discrepancy showing the location of the peak towards higher velocities in experiments is due to the swarm effect, which

is not accounted for in numerical simulations. Although the vertical component of the velocity is mainly dominated by drag and buoyancy forces, the lift force still plays an indirect role by redistributing the bubble momentum through enhanced lateral motion. Accordingly, in the β_L model, higher lift force results in a stronger lateral component of velocity for a larger number of bubbles compared to the Tomiyama model. Consequently, a larger fraction of the total bubble velocity is transferred to the horizontal direction, leading to lower vertical velocity components for many bubbles.

For the horizontal component, the difference between the lift models becomes even more evident. As demonstrated in Fig. 16(b), the PDF obtained using the Tomiyama model is much narrower and more sharply peaked around zero, indicating that most bubbles experience relatively small transverse velocities. This evidently suggests that this model under-predicts lateral dynamics. In contrast, the β_L model produces a broader distribution, which is in much closer agreement with the experimental PDF. This is attributed to the fact that the β_L model dynamically adjusts the lift of individual bubbles based on the local turbulent properties. The Hessenkemper lift model also shows a broad velocity distribution for the lateral velocities, which is in line with the experiments and the β_L model. The reason is that the Hessenkemper lift model makes use of the Legendre lift model for this size range (Legendre and Magnaudet, 1998) that predicts values close to 0.5 for this bubble size range, which is higher compared to what the Tomiyama lift model predicts. The small difference between the PDF curves of the β_L model and the Hessenkemper model is because the upper limit of the C_L value, which is currently proposed in Eq. (30), is higher than that of the Hessenkemper model.

The joint PDFs of the vertical and lateral velocities, $P(u_x, u_z)$, provide further insights into the coupled behavior of the horizontal and vertical velocity components, and allow a more detailed comparison between the experiments and the two lift models. It is evident from Fig. 17 that both the experimental results and the β_L model exhibit a significantly wider spread of the joint probability density in the horizontal direction, whereas the Tomiyama model results in a much more concentrated distribution around $u_x = 0$. This wider distribution directly reflects that a larger portion of bubbles experiences higher transverse velocities in both the experiments and the β_L model. In contrast, the narrow and highly concentrated structure of the joint PDF obtained with the Tomiyama model suggests an under-prediction of lateral dynamics, with most bubbles remaining close to purely vertical trajectories. The results of the Hessenkemper model again show the same trend as before, with quite close agreement with the results of the proposed model.

5. Conclusions

In this research, a new lift model for Euler–Lagrange large eddy simulations of bubbly flows is developed, implemented, and tested for the plumes and columns with a wide range of bubble sizes. The model is rooted in quantities associated with the local hydrodynamic properties of the carrier phase, including the turbulence decay time and a vorticity-based time scale. First, a comprehensive physical analysis of a single-phase jet is performed to postulate a relation between these two time scales and their connection to the coherent and dispersive behavior of the jet. Based on this understanding, a dimensionless parameter (β_L) is introduced as a function of local turbulence characteristics, as well as gas-phase properties, including bubble modified Eotvos number to account for bubble deformation, and the gas void fraction. Then, a new correlation for bubble C_L was found proportional to β_L . The model is implemented in the Euler–Lagrange solver MPPICInterFoam in OpenFOAM. The model performance in representing bubbly flow behavior was evaluated against other lift models derived from single-bubble hydrodynamics over a wide range of bubble sizes (0.5–11 mm), using both literature data and in-house experimental results. For the latter, a bubble plume setup was constructed,

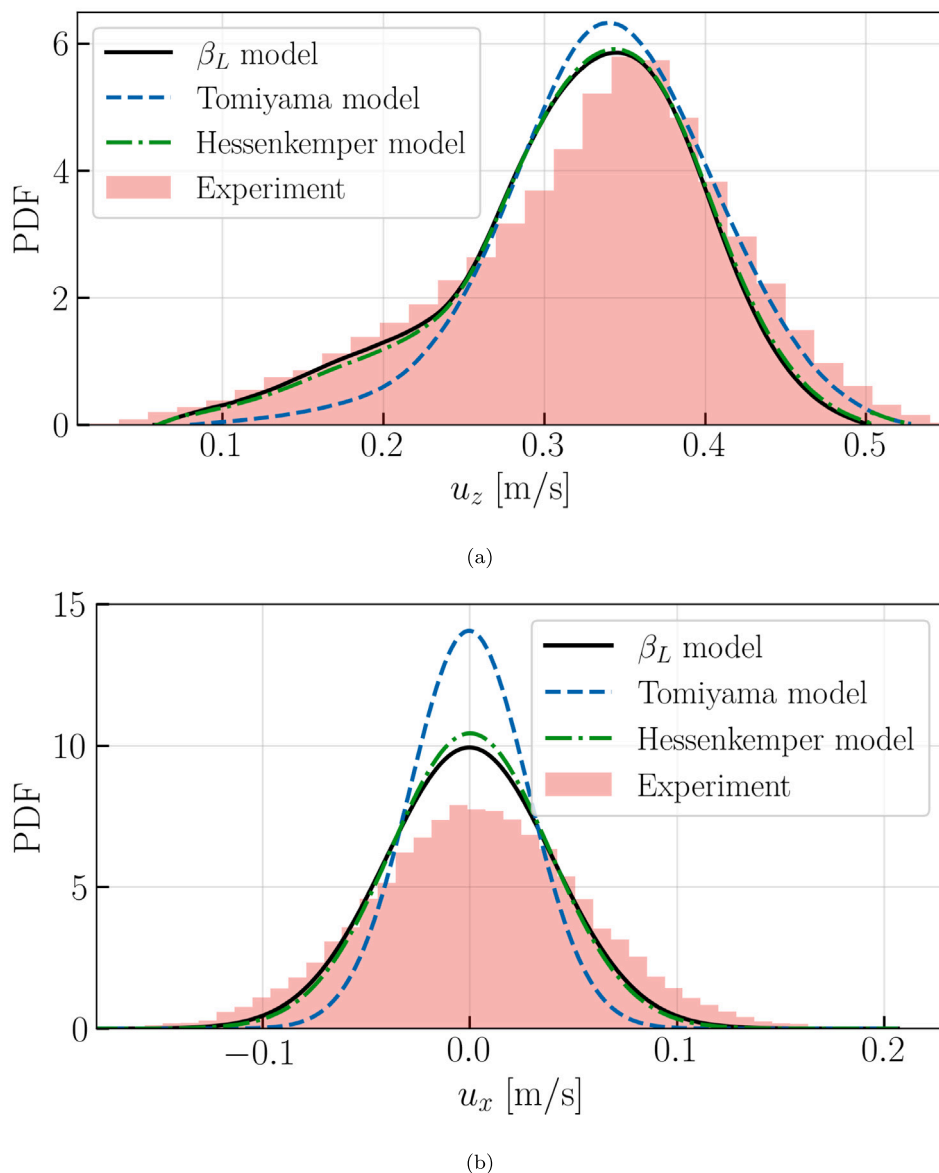


Fig. 16. Comparison of experimental and numerical probability distribution functions (PDFs) of bubble velocities for case Poly-D2: (a) vertical velocity component, u_z , and (b) transversal velocity component, u_x .

and a bubble detection algorithm was developed to extract Lagrangian information on each bubble in the plume. In contrast to the time-averaged profiles often used for model development and validation, these Lagrangian data enable the capture of more detailed information on the lateral motion of bubbles within the plume. The performance analysis showed that the proposed model not only provides the most accurate results, but it is also responsive to the dynamic flow conditions of each setup, as it captures the transition from dispersive to non-dispersive zones in such cases and correctly reflects the change in lift behavior along the plume height.

The original contribution of this research lies in the development of a bubble lift model based solely on turbulent plume physics, represented by a parameter that is dynamically computable within an Euler–Lagrange LES framework. Although the proposed C_L correlation is calibrated using a limited number of plume configurations, the consistent performance of the model over different geometries and column aspect ratios, bubble size ranges, and flow rates indicates a promising level of universality. To our best knowledge, this approach is among the

few successful attempts to replace traditional single-bubble-derived lift models for large-scale industrial applications.

Nevertheless, several important aspects remain to be addressed in future work. In particular, the present physical model is formulated based on the hypothesis that links the lateral motion of Lagrangian bubbles to the turbulence decay time and a local vorticity-based time scale as the bubble exposure time to lift generation. Despite its physical soundness and the accuracy of the results, this hypothesis should still be the subject of further quantification in a canonical flow configuration, such as bubble-laden turbulent channel flow. Also from the modeling viewpoint, further validation over a broader range of operating conditions, including different gas and liquid properties, e.g. steel and argon in metallurgical flows, and more complex conditions such as bubble plumes rising under reduced pressure remain for future research. Moreover, future studies will focus on extending the framework to account for the effects of strong bubble–bubble interactions like bubble coalescence and breakup.

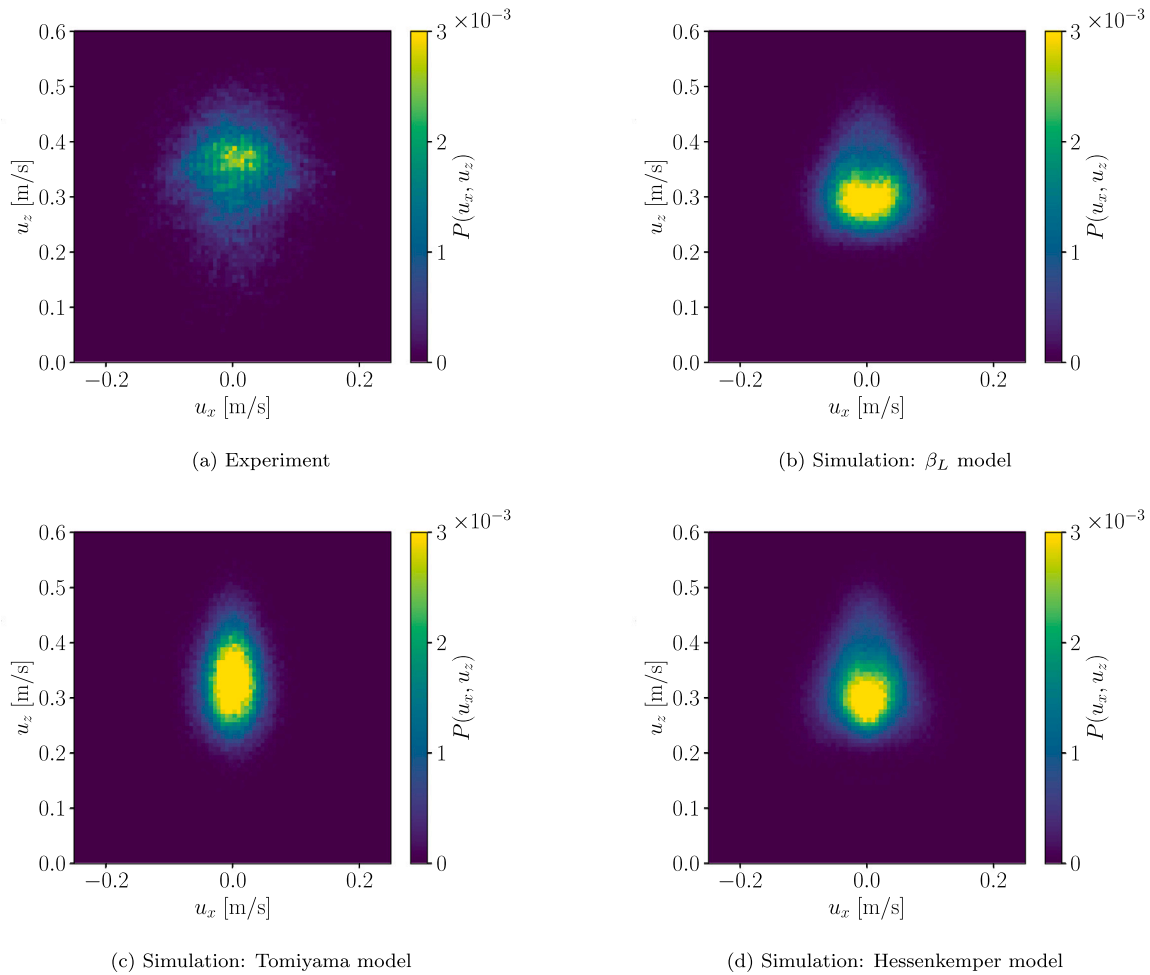


Fig. 17. Joint PDFs of the vertical and lateral bubble velocities, $P(u_x, u_z)$, for Lagrangian bubbles in case Poly-D2: (a) experiment, (b) β_L model, (c) Tomiyama model, and (d) Hessenkemper model.

CRedit authorship contribution statement

Mohammad Karimi Zand: Writing – original draft, Visualization, Validation, Software, Methodology, Investigation, Formal analysis, Data curation, Conceptualization. **Simon Innerbichler:** Visualization, Validation, Software, Methodology, Data curation. **Stefan Putteringer:** Writing – review & editing, Validation, Resources, Methodology, Funding acquisition, Data curation. **Mahdi Saeedipour:** Writing – review & editing, Supervision, Resources, Project administration, Methodology, Investigation, Funding acquisition, Formal analysis, Conceptualization.

Declaration of competing interest

The authors declare the following financial interests/personal relationships which may be considered as potential competing interests: Mohammad Karimi Zand reports financial support was provided by K1-MET GmbH. Stefan Putteringer reports financial support was provided by Austrian Research Promotion Agency. Mahdi Saeedipour reports financial support was provided by European Resuscitation Council. If there are other authors, they declare that they have no known competing financial interests or personal relationships that could have appeared to influence the work reported in this paper.

Acknowledgments

The authors gratefully acknowledge the funding support of K1-MET GmbH, metallurgical competence center. The research program of the

K1-MET competence center was supported by COMET (Competence Center for Excellent Technologies), the Austrian program for competence centers. COMET was funded by the Federal Ministry for Climate Action, Environment, Energy, Mobility, Innovation and Technology, the Federal Ministry for Digital and Economic Affairs, the Federal States of Upper Austria, Tyrol and Styria, as well as the Styrian Business Promotion Agency (SFG). In addition to the public funding from COMET, this research project was partially financed by the industrial partners (voestalpine Stahl Linz GmbH, voestalpine Stahl Donawitz GmbH, and RHI Magnesita GmbH). The last three authors also acknowledge the financial support from the European Research Council (ERC) (grant agreement No. 101160908, FragTuRe). Funded by the European Union. Views and opinions expressed are however those of the author(s) only and do not necessarily reflect those of the European Union or the European Research Council Executive Agency. Neither the European Union nor the granting authority can be held responsible for them.

Data availability

Data will be made available on request.

References

- Adoua, R., Legendre, D., Magnaudet, J., 2009. Reversal of the lift force on an oblate bubble in a weakly viscous linear shear flow. *J. Fluid Mech.* 628, 23–41.
- Antonia, R.A., Satyaprakash, B.R., Hussain, A.K.M.F., 1980. Measurements of dissipation rate and some other characteristics of turbulent plane and circular jets. *Phys. Fluids* 23, 695–700.

- Auton, T.R., 1987. The lift force on a spherical body in a rotational flow. *J. Fluid Mech.* 183, 199–218.
- Besagni, G., Inzoli, F., 2016. Comprehensive experimental investigation of counter-current bubble column hydrodynamics: Holdup, flow regime transition, bubble size distributions and local flow properties. *Chem. Eng. Sci.* 146, 259–290.
- Buwa, V.V., Deo, D.S., Ranade, V.V., 2006. Eulerian-Lagrangian simulations of unsteady gas-liquid flows in bubble columns. *Int. J. Multiph. Flow* 32, 864–885.
- Buwa, V.V., Ranade, V.V., 2002. Dynamics of gas-liquid flow in a rectangular bubble column: experiments and single/multi-group CFD simulations. *Chem. Eng. Sci.* 57, 4715–4736.
- Clift, R., Grace, J.R., Weber, M.E., 1978. *Bubbles, Drops, and Particles*. Academic Press, p. 380.
- de Wit, X.M., Fruchart, M., Khain, T., Toschi, F., Vitelli, V., 2024. Pattern formation by turbulent cascades. *Nature* 627, 515–521.
- Deen, N., 2001. An Experimental and Computational Study of Fluid Dynamics in Gas-Liquid Chemical Reactors (Ph.D. thesis). University of Aalborg, Aalborg University, Denmark.
- Esgandari, B., Schneiderbauer, S., 2025. On grid-independency of CFD-DEM simulations of cluster-induced turbulence. *Int. J. Multiph. Flow* 188, 105223.
- Fatehifar, M., Revell, A., Jabbari, M., De Rosi, A., 2023. A numerical analysis of particle encapsulation in a flow-focusing droplet generation device. *Phys. Fluids* 35 (11), 113317.
- Fraga, B., Stoesser, T., 2016. Influence of bubble size, diffuser width, and flow rate on the integral behavior of bubble plumes. *J. Geophys. Res.: Ocean.* 121, 3887–3904.
- Fraga, B., Stoesser, T., Lai, C.C., Socolofsky, S.A., 2016. A LES-based Eulerian-Lagrangian approach to predict the dynamics of bubble plumes. *Ocean. Model.* 97, 27–36.
- Hayashi, K., Hessenkemper, H., Lucas, D., Legendre, D., Tomiyama, A., 2021. Scaling of lift reversal of deformed bubbles in air-water systems. *Int. J. Multiph. Flow* 142.
- Henriquez-Vargas, L., Donoso-García, P., Lackey, L., Bravo-Gutiérrez, M., Cajas, B., Reyes, A., Pailahueque, N., Díaz-Aburto, I., Bubnovich, V., 2024. Modeling of the solid stress tensor in the MP-PIC method: A review of methods and applications. *Mathematics* 12 (23).
- Hessenkemper, H., Starke, S., Atassi, Y., Ziegenhein, T., Lucas, D., 2022. Bubble identification from images with machine learning methods. *Int. J. Multiph. Flow* 155, 104169.
- Hessenkemper, H., Wang, L., Lucas, D., Tan, S., Ni, R., Ma, T., 2024. 3D detection and tracking of ellipsoidal bubbles in swarms with the aid of deep learning models. *Int. J. Multiph. Flow* 179, 104932.
- Hessenkemper, H., Ziegenhein, T., Rzehak, R., Lucas, D., Tomiyama, A., 2021. Lift force coefficient of ellipsoidal single bubbles in water. *Int. J. Multiph. Flow* 138, 103587.
- Hibiki, T., Ishii, M., 2007. Lift force in bubbly flow systems. *Chem. Eng. Sci.* 62, 6457–6474.
- Homan, T.A.M., Deen, N.G., 2024. Deep Learning Bubble Segmentation on a Shoestring. *Ind. Eng. Chem. Res.* 63 (17), 7800–7806.
- Huang, G., Hessenkemper, H., Tan, S., Ni, R., Sommer, A., Bragg, A.D., Ma, T., 2025. Taylor dispersion of bubble swarms rising in quiescent liquid. *J. Fluid Mech.* 1014, R1.
- Karimpour, F., Venayagamoorthy, S.K., 2013. Some insights for the prediction of near-wall turbulence. *J. Fluid Mech.* 723, 126–139.
- Kubilay, A., Derome, D., Blocken, B., Carmeliet, J., 2015. Numerical modeling of turbulent dispersion for wind-driven rain on building facades. *Environ. Fluid Mech.* 15, 109–133.
- Küçük, S., Della Santina, C., Laskari, A., 2026. Segmenting the complex and irregular in two-phase flows: A real-world empirical Study with SAM2. *Int. J. Multiph. Flow* 196.
- Kulkarni, A.A., 2008. Lift force on bubbles in a bubble column reactor: Experimental analysis. *Chem. Eng. Sci.* 63, 1710–1723.
- Lain, S., Bröder, D., Sommerfeld, M., Göz, M., 2002. Modelling hydrodynamics and turbulence in a bubble column using the Euler-Lagrange procedure. *Int. J. Multiph. Flow* 28 (8), 1381–1407.
- Lamb, H., 1924. *Hydrodynamics*. Cambridge University Press.
- Laupsien, D., Men, C.L., Cockx, A., Liné, A., 2022. Effects of liquid viscosity and bubble size distribution on bubble plume hydrodynamics. *Chem. Eng. Res. Des.* 180, 451–469.
- Legendre, D., Magnaudet, J., 1998. The lift force on a spherical bubble in a viscous linear shear flow. *J. Fluid Mech.* 368, 81–126.
- Lesieur, M., 2008. Turbulence in fluids, 4th revised and enlarged In: *Fluid Mechanics and Its Applications*, vol. 84, Springer Science & Business Media.
- Li, G., Wang, B., Wu, H., DiMarco, S.F., 2020. Impact of bubble size on the integral characteristics of bubble plumes in quiescent and unstratified water. *Int. J. Multiph. Flow* 125, 103230.
- Lucas, D., Krepper, E., Prasser, H.-M., 2007. Use of models for lift, wall and turbulent dispersion forces acting on bubbles for poly-disperse flows. *Chem. Eng. Sci.* 62, 4146–4157.
- Lucas, D., Krepper, E., Prasser, H.-M., Manera, A., 2006. Investigations on the stability of the flow characteristics in a bubble column. *Chem. Eng. Technol.* 29, 1066–1072.
- Lucas, D., Ziegenhein, T., 2019. Influence of the bubble size distribution on the bubble column flow regime. *Int. J. Multiph. Flow* 120, 103092.
- Maeda, K., Date, M., Sugiyama, K., Takagi, S., Matsumoto, Y., 2021. Viscid interactions of pairwise bubbles in a turbulent channel flow and their implications for bubble clustering. *J. Fluid Mech.* 919, A30.
- Martínez Mercado, J., Chehata Gomez, D., van Gils, D., Sun, C., Lohse, D., 2010. On bubble clustering and energy spectra in pseudo-turbulence. *J. Fluid Mech.* 650, 287–306.
- Mathai, V., Huisman, S.G., Sun, C., Lohse, D., Bourgoin, M., 2018. Dispersion of air bubbles in isotropic turbulence. *Phys. Rev. Lett.* 121, 054501.
- Mougin, G., Magnaudet, J., 2006. Wake-induced forces and torques on a zigzagging/spiralling bubble. *J. Fluid Mech.* 567, 185–194.
- Murman, S.M., 2013. A scalar anisotropy model for turbulent eddy viscosity. *Int. J. Heat Fluid Flow* 42, 115–130.
- Saeedipour, M., Schneiderbauer, S., 2025. Enstrophy transport rates determine the Kolmogorov-Hinze scale in turbulent fragmentation of droplets. *Phys. Rev. Fluids* 10, 044301.
- Salibindla, A.K.R., Masuk, A.U.M., Tan, S., Ni, R., 2020. Lift and drag coefficients of deformable bubbles in intense turbulence determined from bubble rise velocity. *J. Fluid Mech.* 894, A20.
- Sankaranarayanan, K., Sundaresan, S., 2002. Lift force in bubbly suspensions. *Chem. Eng. Sci.* 57, 3521–3542.
- Schmidt, U., Weigert, M., Broaddus, C., Myers, G., 2018. Cell detection with star-convex polygons. In: *Medical Image Computing and Computer Assisted Intervention - MICCAI 2018 - 21st International Conference, Granada, Spain, September 16-20, 2018, Proceedings, Part II*. pp. 265–273.
- Schneiderbauer, S., Saeedipour, M., 2019. Numerical simulation of turbulent gas-solid flow using an approximate deconvolution model. *Int. J. Multiph. Flow* 114, 287–302.
- Seol, D.-G., Bhaumik, T., Bergmann, C., Socolofsky, S.A., 2007. Particle image velocimetry measurements of the mean flow characteristics in a bubble plume. *J. Eng. Mech.* 133, 665–676.
- Shang, Z., Liu, H., 2017. Simulating multiphase flows in porous media using openfoam on intel xeon phi knights landing processors. In: *Practice and Experience in Advanced Research Computing 2017: Sustainability, Success and Impact*. pp. 1–7.
- Shi, Z., Jiang, F., Zhao, L., Andersson, H.I., 2022. Scale-dependent particle clustering in transitional wake flow. *J. Fluid Mech.* 940, A4.
- Shu, S., Vidal, D., Bertrand, F., Chaouki, J., 2019. Multiscale multiphase phenomena in bubble column reactors: A review. *Renew. Energy* 141, 613–631.
- Simonnet, M., Gentric, C., Olmos, E., Midoux, N., 2007. Experimental determination of the drag coefficient in a swarm of bubbles. *Chem. Eng. Sci.* 62, 858–866.
- Sokolichin, A., Eigenberger, G., Lapin, A., 2004. Simulation of buoyancy driven bubbly flow: Established simplifications and open questions. *AIChE J.* 50, 24–45.
- Subburaj, R., Tang, Y., Deen, N.G., 2023. An improved lift model for Euler-Lagrange simulations of bubble columns. *Chem. Eng. Sci.* 265, 118182.
- Sugrue, R.M., 2017. A Robust Momentum Closure Approach for Multiphase Computational Fluid Dynamics Applications (Ph.D. thesis). Massachusetts Institute of Technology.
- Tomiyama, A., 2004. Drag, lift and virtual mass forces acting on a single bubble. In: *Third International Symposium on Two-Phase Flow Modeling and Experimentation*. pp. 22–24.
- Tomiyama, A., Kataoka, I., Zun, I., Sakaguchi, T., 1998. Drag coefficients of single bubbles under normal and micro gravity conditions. *JSME Int. J. Ser. B* 41, 472–479.
- Tomiyama, A., Tamai, H., Zun, I., Hosokawa, S., 2002. Transverse migration of single bubbles in simple shear flows. *Chem. Eng. Sci.* 57, 1849–1858.
- Tryggvason, G., Lu, J., 2015. Direct numerical simulations of bubbly flows. *Mech. Eng. Rev.* 2, 15–00220.
- Weigert, M., Schmidt, U., 2022. Nuclei instance segmentation and classification in histopathology images with stardist. In: *The IEEE International Symposium on Biomedical Imaging Challenges*. ISBIC.
- Weigert, M., Schmidt, U., Haase, R., Sugawara, K., Myers, G., 2020. Star-convex polyhedra for 3D object detection and segmentation in microscopy. In: *The IEEE Winter Conference on Applications of Computer Vision*. WACV.
- Wu, H., Wang, B., DiMarco, S.F., Tan, L., 2021. Impact of bubble size on turbulent statistics in bubble plumes in unstratified quiescent water. *Int. J. Multiph. Flow* 141, 103692.
- Xue, J., Chen, F., Yang, N., Ge, W., 2017. A study of the soft-sphere model in Eulerian-Lagrangian simulation of gas-liquid flow. *Int. J. Chem. React. Eng.* 15, 20160064.
- Yoshizawa, A., 1986. Statistical theory for compressible turbulent shear flows, with the application to subgrid modeling. *Phys. Fluids* 29, 2152–2164.
- Zakari, A.G., Mainul Hoque, M., Ireland, P., Evans, G., Mitra, S., 2025. Dynamics of gas dispersion in a rising bubble plume in presence of surfactant. *Miner. Eng.* 222, 109145.
- Zand, M.K., Puttinger, S., Saeedipour, M., 2025. A new approach to unravel the lift force phenomenon of a single bubble rising in stagnant and sheared liquids. *Int. J. Multiph. Flow* 188, 105219.
- Zhang, D., Deen, N., Kuipers, J., 2006. Numerical simulation of the dynamic flow behavior in a bubble column: A study of closures for turbulence and interface forces. *Chem. Eng. Sci.* 61, 7593–7608.
- Zhang, X., Wang, J., Wan, D., 2020. Euler-Lagrange study of bubble drag reduction in turbulent channel flow and boundary layer flow. *Phys. Fluids* 32, 027101.
- Zhang, H., Zhang, W., 2022. Numerical simulation of bubbly jets in crossflow using OpenFOAM. *Phys. Fluids* 34, 123305.